Corrosion Science 229 (2024) 111867

Contents lists available at ScienceDirect

Corrosion Science

journal homepage: www.elsevier.com/locate/corsci

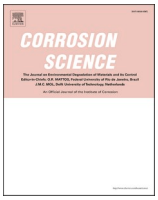

Corrosion inhibition mechanism of 2,6-pyridinedicarboxylate depending on magnesium surface treatment

Ci Song [a,*], Cheng Wang [a,e], Dimitri Mercier [b], Bahram Vaghefinazari [a], Antoine Seyeux [b], Darya Snihirova [a], D.C.F. Wieland [c], Philippe Marcus [b], Mikhail L. Zheludkevich [a,d], Sviatlana V. Lamaka [a]

[a] Institute of Surface Science, Helmholtz-Zentrum Hereon, 21502 Geesthacht, Germany
[b] Chimie ParisTech-CNRS, PSL Research University, Institut de Recherche de Chimie Paris (IRCP), Physical Chemistry of Surfaces Group, 75005 Paris, France
[c] Institute of Metallic Biomaterials, Helmholtz-Zentrum Hereon, Geesthacht 21502, Germany
[d] Institute of Materials Science, Faculty of Engineering, Kiel University, 24143 Kiel, Germany
[e] School of Materials Science and Engineering & Jiangsu Key Laboratory for Advanced Metallic Materials, Southeast University, Nanjing 211189, China

ARTICLE INFO

Keywords:
2,6-pyridinedicarboxylate
Magnesium
Corrosion inhibitor
ToF-SIMS
XPS
Scanning electrochemical microscopy

ABSTRACT

2,6-pyridinedicarboxylate (2,6-PDC) was studied as corrosion inhibitor for pure magnesium. The surface was prepared either by polishing or polishing followed by treatment with 1 M NaOH solution. The results show that 2,6-PDC promotes the formation of a denser protective oxide/hydroxide layer poor in PDC. The mechanism proposed includes forming weak PDC-Mg complexes that lower the free Mg^{2+} concentration available for the formation of $Mg(OH)_2$. This leads to growth of smaller $Mg(OH)_2$ platelets that are more densely packed and hence form a more protective layer. The highest inhibition efficiency of 2,6-PDC was achieved for samples with surface hydroxylated by NaOH treatment.

1. Introduction

Magnesium (Mg) and its alloys have attracted significant attention due to their low density, high specific strength, electromagnetic shielding, biodegradability, recyclability, etc.[1–4]. However, the limited corrosion resistance of Mg alloys remains a problem to overcome in various fields, such as transportation, electronics, biomaterials, and battery applications. Surface modification, including the incorporation of corrosion inhibitors into organic and inorganic coatings, is a common method of improving the corrosion resistance of engineering parts made of various alloys [2], including magnesium, e.g. [2,5–7].

Many compounds have been explored and identified as excellent corrosion inhibitors for Mg alloys [5,8–10]. Corrosion inhibitors can be classified as anodic, cathodic, or mixed-type inhibitors, depending on whether they suppress anodic, cathodic, or both corrosion reactions on metal surfaces [11,12]. Anodic inhibitors are mainly adsorbed on the metal, oxide, or hydroxide surface via electrostatic interaction or complex formation with Mg^{2+}, which forms a passivating layer on the Mg surface, thus suppressing the anodic dissolution of Mg alloys [13]. Hu *et al.* reported that 2-hydroxy-4-methoxy-acetophenone as an inhibitor could form a paeonol-Mg complex mixing with the original $Mg(OH)_2$ film on the Mg surface and inhibit the anodic dissolution of AZ91D [14]. Sodium dodecylbenzene sulfonate (SDBS), a known inhibitor [15], its DBS^- ion competes with Cl^- for accessing Mg surface during corrosion and possesses stronger electrostatic attraction with the Mg matrix [15,16]. Afterward, the long hydrophobic chain in the SDBS molecule hinders the contact of the aggressive solution and the substrate, thus inhibiting Mg corrosion [16].

Inhibitors can be incorporated into various coatings and further improve the corrosion resistance of Mg [17]. Recent review summarizes several types of corrosion inhibitors [12] and their combinations with organic and inorganic layers formed by PEO/MAO or sol-gel techniques, incorporated into Layered Double Hydroxides (LDH) or other carriers [12]. Many inhibitors are able to form conversion coatings on magnesium alloys. Conversion coatings based, among other, on chromate (currently being out-phased), phosphates (with Ca^{2+}, Zn^{2+}, Sr^{2+}, Mn^{2+}), fluorides, cerium and lanthanum salts, stannates, and Mg-organic complexes were reviewed by Vaghefinazari et al. [18]. One of the highly desirable features of coatings loaded with inhibitors is their "active protection" properties. For example, Calado *et al.* incorporated

* Corresponding author.
E-mail address: ci.song@hereon.de (C. Song).

https://doi.org/10.1016/j.corsci.2024.111867
Received 7 November 2023; Received in revised form 11 January 2024; Accepted 20 January 2024
Available online 23 January 2024

cerium tri(bis(2-ethylhexyl)phosphate) ($Ce(DEHP)_3$) into an epoxy-silane hybrid coating to protect AZ31 alloy [19]. The results showed that $Ce(DEHP)_3$ serves as a pH-sensitive inhibitor: the alkalinization due to the Mg corrosion dissociates the $Ce(DEHP)_3$ molecules, which leads to the formation of protective Ce- and P-containing layers.

It is known that noble impurities play a significant role in Mg corrosion due to their highly negative electrode potential. It has been found that noble metallic impurities, especially Fe, accelerate the anodic dissolution of Mg due to the micro-galvanic coupling with Mg matrix [20]. The Fe tolerance limit for high purity cast Mg is around 170 ppm, with even lower concentrations causing severe corrosion, depending on amount of other impurities, especially Si, Al, Mn and Zr and thermal treatment that often leads to segregation of Fe-rich impurities [4,21,22]. Once the Fe content in Mg alloys exceeds their tolerance limit, Fe-rich particles are formed within the Mg matrix. According to Williams *et al.* [20], Fe impurity acts as a persistent cathode during Mg corrosion, and the formation as well as the propagation of dark regions on the Mg surface, which are commonly observed during corrosion, are intimately related to Fe content. At the same time, Höche *et al.* found that when the anodic dissolution of Mg occurs, noble metallic impurities are dissolved and experience "self-corrosion"; eventually, these impurities become ions and re-deposit onto the substrate [23]. Recently, Mercier *et al.* demonstrated, by ToF-SIMS chemical images, the segregation of these iron particles at the grain boundaries during the corrosion process [24] and confirmed their major role in the Mg corrosion mechanism [25]. Following this concept, the cathodic inhibitors hinder the cathodic reaction and limit the anodic reaction. Lamaka *et al.* elucidated that Fe^{II}/Fe^{III} complexing agents (e.g., salicylate, cyanide, and oxalate) could be used as cathodic inhibitors [26]. These cathodic inhibitors prevented the re-plating of iron and greatly inhibit Mg corrosion. Then, Lamaka *et al.* also screened the corrosion inhibition effects of 151 individual chemical compounds towards six Mg alloys (AZ31, AZ91, AM50, WE43, ZE41, and Elektron 21) and three grades of pure Mg. Many compounds were preselected based on their ability to form stable complexes with $Fe^{II}/^{III}$ [5]. Some with universal corrosion inhibition effect to all tested Mg alloys, e.g. fumarate and several derivatives of pyridinedicarboxylate (2,5-PDC; 2,6-PDC; 3,4-PDC; 2,3-PDCA), while other inhibitors were selective to the alloy groups (e.g. thiosalicylate for aluminum-containing Mg alloys, 5-methylsalicylate for rare-earth-containing Mg alloys and salicylate for pure Mg with active iron-rich cathodic intermetallic particles). Following this, Maltseva *et al.* tested sodium salicylate, 2,5-PDC, and fumarate on high purity Mg and commercial purity Mg in NaCl aqueous solution [27]. The results showed that the inhibition efficiency (IE) of these carboxylate inhibitors is influenced by iron contents because of the different amounts of Mg $(OH)_2$ produced during the initial corrosion stage. More importantly, based on Raman spectra in the range of -OH vibrations and SEM micrographs it was shown that addition of all these inhibitors results in the decrease of the size of $Mg(OH)_2$ crystals, hence resulting in denser and more protective layer of corrosion products. Following this discovery, Cui *et al.* investigated the effect of several inhibitors (sodium dodecyl sulfate, benzalkonium chloride, and polyethylene glycol trimethyl nonyl ether) on AZ91D Mg alloy and confirmed that the inhibitor anions adsorb on $Mg(OH)_2$ nuclei with positive charges, resulting in the acceleration of the nucleus growth and the formation of a dense corrosion product layer [28].

Pyridinedicarboxylate (PDC) was found to have a strong inhibiting effect on all tested Mg alloys in [5] where it was reported for the first time. It is known that PDCs are tridentate ligands forming rather strong chelates with $Fe^{II/III}$ and weak complexes with Mg^{2+} [5,29]. Also, Lamaka *et al.* found that a group of PDCs (2,6-, 2,5-, 2,3-, and 3,4-PDC) showed high IE values on six tested alloys and pure Mg [5]. Yang et al. reported that 2,5-pyridinedicarboxylate (2,5-PDC) and fumarate show certain anodic inhibiting behavior on commercially pure magnesium (CP Mg) in NaCl solution, and they increase the open circuit potential of CP Mg during immersion, which means 2,5-PDC forms a passive film on Mg surface [30]. However, Vaghefinazari *et al.* [31] and Zhang *et al.* [32] found that after introducing 2,5-PDC into PEO coating, the overall corrosion resistance decreased instead of increasing. Vaghefinazari confirmed that 2,5-PDC inhibits the corrosion of AZ21 Mg and the IE increases with the increase of concentration, but it forms soluble complexes with Mg^{2+} dissolving $Mg_3(PO_4)_2$, one of the main phases in the PEO coating, and resulting in the deterioration of PEO coating [31]. On the other hand, after the penetration of corrosive electrolyte through the PEO coating, the formation of a protective corrosion product between 2,5-PDC and Mg^{2+} was identified [31]. Similar to 2,5-PDC, [31] also briefly introduced that 2,6-pyridinedicarboxylate (2,6-PDC) promotes formation of corrosion products on the Mg surface, resulting in a thicker corrosion product layer. Therefore, it is necessary to explore the detailed inhibition mechanism of PDCs as promising candidates for the corrosion inhibition of Mg and its alloys. 2,6-PDC was studied in more detail in this work. To understand the influence of surface hydroxylation on the inhibition behavior of 2,6-PDC, either polished or polished and NaOH-treated CP-Mg samples were used in this work. Advanced surface characterization by XPS and ToF-SIMS along with electrochemical methods, namely EIS local electrochemical micro-probes (for measuring local concentration of dissolved molecular hydrogen and oxygen) were employed to investigate the corrosion inhibition effect of 2,6-PDC on CP-Mg in NaCl solution.

2. Experiments

2.1. Materials and reagents

As-cast commercially pure Mg (CP-Mg) was studied as the magnesium substrate. The elemental composition determined by Spark OES (Spark analyzer M9, Spectro Ametek, Germany) is presented in Table 1. Mg samples (10 mm × 10 mm × 3 mm) were first ground with emery papers up to 2500 grit and then polished. Polishing was applied on a polishing disc (80 r/min) with diamond slurry (1 μm diameter) and oxide polished suspension (OPS) solution. Then, samples were rinsed with deionized water and ethanol, and eventually dried in pressured air flow at room temperature. After polishing, one batch of samples was used for later corrosion experiments and another batch of samples was treated with NaOH solution. For NaOH treatment, the tested surface of the sample was kept upward and immersed in 1 M NaOH solution for 10 min with stirring, followed by rinsing with ethanol to remove residual NaOH solution, and then dried by pressured air flow.

The inhibitor used in this work is 2,6-pyridinedicarboxylic acid (2,6-PDCA) ($C_7H_5NO_4$, ACS reagent>98%, Sigma-Aldrich Chemie GmbH, Germany). The inhibitor was dissolved in aqueous 0.5 wt% NaCl solution and the inhibitor concentration was 50 mM. NaOH (1 M) solution was used to adjust the pH value of the solution to 6.8. The pH value of the prepared solution was monitored by Metrohm 691 pH meter. Because of the addition of NaOH, 2,6-PDCA was deprotonated to the soluble sodium salt of 2,6-pyridinedicarboxylate (2,6-PDC) in solution, thus 2,6-PDC is denoted as the inhibitor hereafter. The structural formula of 2,6-PDC is shown in Fig. 1 **(a)**.

2.2. X-ray photoelectron spectroscopy (XPS) and time-of-flight secondary ions mass spectrometry (Tof-SIMS) analysis

XPS characterization was performed using a Thermo ESCALAB 250 X-Ray photoelectron spectrometer with a monochromatic Al Kα X-Ray source ($h\upsilon = 1486.6$ eV) operating at a pressure around 2×10^{-9} mbar. Beforehand the spectrometer was calibrated using Au4f7/2 at 84.1 eV. For each sample, a survey (at 50 eV pass energy) and high-resolution spectra (at 20 eV pass energy) for characteristic photopeaks (Mg2p, Cl2p, C1s, N1s, O1s, Mg1s, Na1s) and Mg Auger transition have been recorded. Charging effects were not compensated in this study and all spectra are presented without binding energy correction. The decomposition of high-resolution spectra has been carried out using Avantage

Table 1
The elemental composition of CP-Mg.

Element, wt%	Fe	Si	Mn	Al	Cu	Ni	Ca or Ag	Mg
CP-Mg for XPS, TOF-SIMS and corrosion experiments	0.0342	0.00010	0.00237	0.00402	0.00037	< 0.00020	-	Bal.
CP-Mg for XRD	0.0178	< 0.00010	0.00416	0.0268	0.00067	0.00032	< 0.00010	Bal.

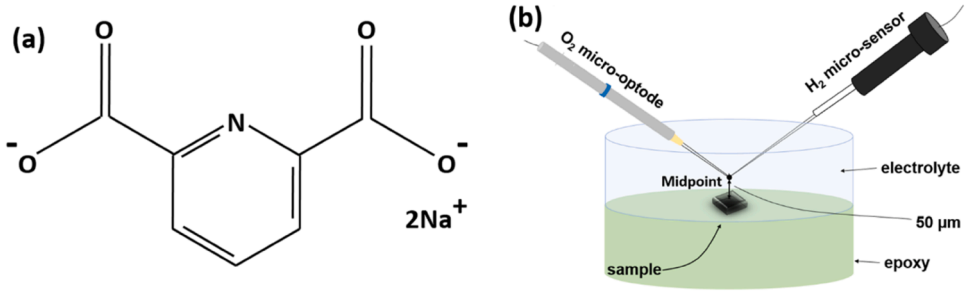

Fig. 1. **(a)** the formula structure of 2,6-pyridinedicarboxylate sodium salt; **(b)** the schematic setup for simultaneous measurements of local concentration of dissolved molecular hydrogen and oxygen.

software.

Determination of atomic composition and the atomic fraction of each species is obtained using Eq. 1 [25]. Assuming that the layer is homogeneous and distinct, a 3-layer model consisting of a $MgCO_3$/Mg $(OH)_2$/MgO stack could be used [33]. Thicknesses have been obtained solving the set of Eqs. (2, 3, 4, and 5) [33,34]:

$$X(at\%) = \frac{100\frac{I(X)}{\lambda_X \sigma_X T_X}}{\sum \frac{I_i}{\lambda_i \sigma_i T_i}} \quad (1)$$

$$I(MgCO3) = n_{MgCO3}\sigma_{Mg2p}T_{Mg2p}\lambda_{Mg2p}^{MgCO3}\left(1-\exp\left(-\frac{d_{MgCO3}}{\lambda_{Mg2p}^{MgCO3}}\right)\right) \quad (2)$$

$$I(Mg-OH) = n_{Mg(OH)2}\sigma_{Mg2p}T_{Mg2p}\lambda_{Mg2p}^{Mg(OH)2}\exp(-\frac{d_{MgCO3}}{\lambda_{Mg2p}^{MgCO3}})(1-\exp\left(-\frac{d_{Mg(OH)2}}{\lambda_{Mg2p}^{Mg(OH)2}}\right) \quad (3)$$

$$I(Mg-O) = n_{MgO}\sigma_{Mg2p}T_{Mg2p}\lambda_{Mg2p}^{MgO}(1-\exp\left(-\frac{d_{MgO}}{\lambda_{Mg2p}^{Mgo}}\right))\exp(-\frac{d_{Mg(OH)2}}{\lambda_{Mg2p}^{Mg(OH)2}})\exp(-\frac{d_{MgCO3}}{\lambda_{Mg2p}^{MgCO3}}) \quad (4)$$

$$I(Mg) = n_{Mg}\sigma_{Mg2p}T_{Mg2p}\lambda_{Mg2p}^{Mg}\exp\left(-\frac{d_{MgO}}{\lambda_{Mg2p}^{MgO}}\right)\exp\left(-\frac{d_{Mg(OH)2}}{\lambda_{Mg2p}^{Mg(OH)2}}\right)\exp\left(-\frac{d_{MgCO3}}{\lambda_{Mg2p}^{MgCO3}}\right) \quad (5)$$

where I is the peak intensity measured for each species, λ is the inelastic mean free path (nm), σ is the Scofield factor, T is the transmission factor of the spectrometer and d is the layer thickness. X indicates specific species. Values of inelastic mean free path and σ are obtained from [34–37]. Through the Eq. 1, the atomic fraction of different species could be obtained. Layer thickness could be determined by Equation 2~5.

Table 2
Characteristic fragments used during ToF-SIMS analysis.

Ions	Mass (amu)	Ions	Mass (amu)
$MgOH^-$	40.9878	$C_8H_7O_3^-$	151.0395
MgO_2^-	55.9749	$C_7H_7O_2Mg^-$	147.0297
MgH^-	24.9929	$C_8H_7O_3MgO^-$	191.0195
$^{25}MgH^-$	25.9937	$C_8H_7O_3MgOH^-$	192.0273
CO_3^-	59.9848	$C_6H_3NO_2MgOH^-$	162.0041
Cl^-	34.9689	$C_7H_4NO_4MgO^-$	205.9940
Na^-	22.9898		

ToF-SIMS analysis was performed using a ToF-SIMS V spectrometer (ION TOF GmbH, Munster, Germany) operating at 10^{-9} mbar pressure. The spectrometer was run in HC-BUNCHED mode to get a high mass resolution (M/ΔM around 8000). Negative ions depth profiles were performed by sequentially analyzing (Bi^+, 1.2 pA, 100 × 100 μm^2) and sputtering (Cs^+, 500 eV, 20 nA, 500 × 500 μm^2) the sample surface. Both guns have a 45° incidence angle with respect to the specimen surface. The Bi ion flux was kept below 10^{-12} ions.cm^{-2} to ensure quasi static conditions. Data acquisition and post-processing analyses were performed using Ion-Spec software (version 6). The fragments used during this study and their assignments are listed in Table 2.

In XPS and ToF-SIMS measurements, samples were first treated as described in **Section 2.1** . Half of the samples were tested for XPS and ToF-SIMS directly, the other half of the samples were immersed in NaCl solutions (0.5 wt%) with or without 2,6-PDC (50 mM) for 15 min. After immersion, these samples were cleaned with deionized water and ethanol and then dried by pressured air flow for later XPS and ToF-SIMS measurements. The reason we used samples after 15 min for XPS and ToF-SIMS is to investigate the effect of 2,6-PDC on Mg surface during the initial corrosion process that forms the condition for corrosion inhibition while still remaining within layer roughness allowing accurate quantification.

2.3. X-ray diffraction (XRD)

XRD measurements were performed at the side station of the beamline P07 at the PETRA III storage ring, Deutsches Electron Synchrotron, DESY, Hamburg, Germany [38]. For the experiment, an in-house developed sample cell was used that allowed capturing XRD patterns while the sample was in liquid and polarized. In this way the formation of crystalline products could be followed in situ. The samples were polished CP-Mg immersed in 3.5 wt% NaCl solution under cathodic polarization with a 5 mA/cm^2 current density. Prior to the measurements, the surface was prepared as described in 2.1. The measurements started as soon as the sample got in contact with the solution and XRD data were collected every 5 s for a total duration of 1 h in total. The measurements were performed at a grazing angle of 1° to have a maximum signal from the surface. The X-ray beam energy was 87 keV with a wavelength of 0.145 Å. A Perkin Elmer detector was used. The scattering angle 2θ of the diffraction patterns was converted to Cu K-alpha radiation to better compare to the literature.

2.4. Scanning electron microscope (SEM)

The morphology of the samples after immersion in the NaCl solution with and without 2,6-PDC was characterized by SEM (LYRA3 TESCAN), the acceleration voltage was 15 kV. Polished samples were used in this part. The specimens were pre-immersed in NaCl with or without 2,6-PDC or 2,5-PDC for 30 min to make sure the corrosion product layer was fully formed, then cleaned with deionized water, ethanol to remove the corrosive solution and dried in a stream of warm air. The corroded surfaces of CP-Mg were sputtered with gold before observation using a Cressington Sputter Coater 108 auto Cross-sections were prepared by FIB milling, integrated into LYRA3 TESCAN.

2.5. Electrochemical measurements

All electrochemical measurements were performed in NaCl solution (0.5 wt%) with or without 2,6-PDC. A conventional three-electrode system with Gamry Interface 1010 potentiostat was employed, which includes a reference electrode (saturated KCl electrode), counter electrode (coiled platinum wire electrode), and working electrode (Mg samples with 1 cm^2 exposed surface area). Prior to the electrochemical impedance spectroscopy (EIS) test, the samples were stabilized in solution for 10 to 15 min to achieve relatively stable potential. The scanned frequency ranged from 10^5 to 10^{-1} Hz, 10 points per decade, and a sinusoidal amplitude of 10 mV_{rms}. The EIS spectra were continuously measured to follow up the progress of the corrosion/inhibition processes within 24 h frame. All the measurements were repeated at least three times and performed at room temperature (22 ± 1 °C).

In this study, the non-inhibited system demonstrated non-stationarity. The Gamry Framework software offers a “fast mode” option for EIS tests, specifically tailored for similar scenarios where the stability of the system under study is not guaranteed. Using this mode, the duration of EIS can be reduced by about 3 times in average. Therefore, any drift of OCP during the EIS measurements is effectively reduced. Furthermore, to keep the EIS measurement time efficient while still capturing relevant data, the frequency range for these measurements was therefore limited to a minimum of 10^{-1} Hz.

2.6. Hydrogen evolution measurements

Hydrogen evolution experiments were performed using eudiometers (art. nr. 2591–10-500 from Neubert-Glas, Germany). This kind of eudiometers can prevent the access of other gases from the ambient environment. The hydrogen evolution setup was also reported in our previous work [39]. In this setup, the weight of water displaced from the eudiometer due to the evolved hydrogen was measured by a balance (Sartorius AX224) and the value was recorded automatically every 5 min using USB data logger (OHAUS, 30268984). By this method, the accuracy of data is increased due to continuous data-logging and excluding the errors of manual recording. Only one sample with the surface area of 200 ± 20 mm^2 was placed in each eudiometer bottle with 500 mL of solution. Before the hydrogen evolution, the solutions were purged with hydrogen and argon mixtures for 20 min to ensure the pre-saturation with hydrogen and decrease the concentration of dissolved oxygen. For each sample, all six surfaces were ground up to 2500 grit and polished as described in **Section 2.1** and then directly used in later hydrogen evolution experiments or treated by NaOH solution. During the test period, the electrolyte was constantly agitated by a magnetic stirrer. All experiments were repeated at least three times for reproducibility. Using hydrogen evolution, the inhibition efficiencies (IEs) of 2,6-PDC for different surface-treated samples were calculated by Eq. 6. The error of IE calculated by H_2 evolution is calculated by Eq. 7.

$$IE_{H_2} = \frac{V_{H_2}^{NaCl} - V_{H_2}^{Inh}}{V_{H_2}^{NaCl}} \tag{6}$$

$$\Delta IE_{H_2} = \frac{V_{H_2}^{Inh} \times \Delta V_{H_2}^{NaCl}}{V_{H_2}^{NaCl^2}} + \frac{\Delta V_{H_2}^{Inh}}{V_{H_2}^{NaCl}} \tag{7}$$

2.7. Measuring local concentration of dissolved molecular hydrogen (DH) and dissolved oxygen (DO) using scanning electrochemical microscopy

A schematic of the cell for scanning electrochemical microscopy is shown in Fig. 1 **(b)**. The local concentration of dissolved molecular hydrogen (DH) and oxygen (DO) were measured by Clark type amperometric microelectrode and micro-optode, respectively. Samples with two different surface treatments were sealed with beeswax, except for a square area of 10 × 10 mm^2 exposed to the testing electrolyte. The volume of electrolyte was around 5 mL, staying 5 mm above the sample surface in a custom-made cell designed for the local measurements. The local concentration of the DH was measured using a H_2 microsensor (10 μm tip diameter, H_2-10) connected to an fx-6 UniAmp (both from Unisense, Denmark). A retractable fiber-optic oxygen micro-optode (50 μm tip diameter, OXR50-UHS), coupled with an oxygen concentration meter FireStingO_2 (both from Pyroscience™, Germany) were employed to monitor the DO concentration. Both H_2 microsensor and O_2 micro-optode were calibrated considering the salinity and temperature of the solution. The DH and DO local concentrations were measured simultaneously, using a custom-made dual-head stage, at the height of 50 μm above the midpoint of the specimen surface. Both probes were integrated into a commercial SVET-SIET system from Applicable Electronics™ for data acquisition by LV4 software from Sciencewares™ in parallel with PyroOxygenLogger from Pyroscience™.

3. Results

3.1. XPS

Fig. 2 shows the Mg2p (**(a)** and **(b)**), O1s (**(c)** and **(d)**), and C1s (**(e)** and **(f)**) decomposition spectra for polished Mg (**(a)**, **(c)**, and **(e)**) and

Table 3
Atomic composition of surface layer obtained by XPS for the Mg after different surface treatments.

Atomic composition (%)	C1s				Mg2p			O1s				Na1s
	C-C	C-O	COOH	$MgCO_3$	Mg	MgO_x	$MgCO_3$	MgO	Mg-OH	cont.	$MgCO_3$	
Polished Mg	7.0	1.1	1.4	6.4	7.6	17.0	6.4	7.1	24.2	3.9	17.9	–
NaOH Mg	15.2	1.0	0.8	1.8	–	24.4	1.8	–	46.1	2.6	5.0	0.7

*cont.: contamination

Table 4
Thickness of the two layers (nm) measured by XPS for the samples after different surface treatments.

Thickness (nm)	MgO	$Mg(OH)_2$	$MgCO_3$
Polished Mg	2.0	0.9	2.0
NaOH Mg	–	> 12	0.3

NaOH-treated Mg samples (**(b)**, **(d)**, and **(f)**). For Mg2p spectra, three distinct components characteristic of Mg (49.6 eV) $MgO/Mg(OH)_2$ (51.3 eV) and $MgCO_3$ (52 eV) are observed on polished Mg while only a component characteristic of $MgO/Mg(OH)_2$ at 51.7 eV and $MgCO_3$ at 52.7 eV are visible on the surface of NaOH-treated Mg sample. For the O1s high-resolution spectrum, three components assigned to $MgCO_3$ (533.8 eV-polished), Mg-O (531.3 eV-polished), and Mg-OH (533 eV) are presented on polished Mg and only two for the NaOH-treated surface. The absence of Mg-O component indicates the growing of the hydroxide Mg layer. In the C1s spectrum, peaks observed are associated with the presence of contamination, including hydrocarbons and carbonates. The component at high binding energy is characteristic of the carbonate species and is mainly present on polished samples. The atomic composition of different species for different samples is shown in Table 3. The amount of $Mg(OH)_2$ on NaOH-treated Mg samples is clearly greater than that on polished samples. Then the layer thickness of two samples is calculated according to Equation 2-eq**. 4** and listed in Table 4. The total layer thickness of polished Mg is around 4.9 nm (of which MgO accounts to 2.0 nm). Owing to the excessive thickness of $Mg(OH)_2$ layer for the NaOH-treated sample, it is not possible to determine the thickness of its MgO layer by XPS. Complete attenuation of the substrate signal only means the hydroxide layer thickness is greater than 12 nm. Therefore, ToF-SIMS was used to measure the layer thickness of the NaOH-treated sample. This thicker layer can explain the small energetic shift observed for the NaOH treatment.Fig. 2.

The evolution of characteristic photopeaks (C1s **(a)**, Mg2p **(b)**, and O1s **(c)**) for two samples after 15 min immersion in NaCl solution and the corresponding Mg2p spectra with peak fitting (polished **(d)** and NaOH-treated **(e)** samples) are presented in Fig. 3. The Mg2p **(a)**, O1s **(b)**, and C1s **(c)** spectra for polished Mg and NaOH-treated Mg samples are presented in Fig. 4. For all samples, the peaks are shifted towards higher binding energies suggesting a more insulating behavior probably caused by a thickening of the oxide or/and hydroxide layer or denser layer formed in line with previous conclusion [27]. This hypothesis is confirmed by the disappearance of the metallic component and Mg-O component observed in the Mg2p fitted spectrum on NaOH-treated sample (Fig. 4 **(e)** and **(g)**). Thus, the surfaces analyzed after NaCl with or without 2,6-PDC immersion are composed mainly of $Mg(OH)_2$ with a thickness larger than 12 nm. Additionally, after 15 min of immersion in 2,6-PDC, the signals of COO^- or COOH species are presented in Fig. 4 **(d)** and **(e)**, suggesting the 2,6-PDC species remain on the surface of the corrosion product layer when samples are immersed into the inhibitor solution. However, it is unclear whether 2,6-PDC is involved in the formation of the corrosion product layer because the detection depth of XPS is not deep enough. Therefore, ToF-SIMS should be used to detect the components of the formed corrosion product layer in NaCl solution with and without 2,6-PDC.

3.2. ToF-SIMS

Because XPS cannot detect the thickness of a layer that is too thick, ToF-SIMS was employed for measuring too thick layer. Fig. 5 shows the ToF-SIMS depth profiles of negative fragments obtained for polished **(a)** and NaOH-treated **(b)** samples before immersion in the NaCl solution. The position of the metal-oxide interface is determined from the decrease in the MgO_2^- signal that is characteristic of MgO [25]. Thus, the oxidized Mg layer thickness, covering the metallic substrate, corresponds to ~ 4 nm and ~ 47 nm for polished Mg and NaOH-treated Mg substrate, respectively (the constant sputtering rate is 0.16 nm/s, determined from a mechanical profilometry measurement after profiling). From the position of the MgO^{2-}, $MgOH^-$ and CO_3^{2-} signals (characteristic species for Mg oxide, Mg hydroxide and Mg carbonates, respectively), it can be concluded that the oxide scale corresponds to a bilayer structure with an inner MgO layer covered by an outer layer composed of $Mg(OH)_2$ and $MgCO_3$. From the intensity of the $MgOH^-$, it is also concluded that the content of $Mg(OH)_2$ in the NaOH-treated sample is higher than that in the polished one. For both samples, Cl^- signals are detected on the extreme outer surface. However, knowing that the samples are not exposed to Cl^- containing solutions, that Cl^- ion is very sensitive in negative polarity and that Cl^- is not detected by XPS (meaning concentration <0.5 at%), the Cl^- signal on the outer surface is assigned to contamination although it shows a rather high intensity in the ToF-SIMS depth profiles due to high ionization yield in negative polarity.

The ToF-SIMS depth profiles on **(a)** polished and **(b)** NaOH-treated samples after exposure to NaCl solution for 15 min are presented in Fig. 6. Looking at the $MgOH^-$ signals, characteristic of $Mg(OH)_2$, their maximum intensities are reached for 294 nm and 214 nm for the polished and NaOH-treated samples (shown in Table 5), respectively, which are also located before the MgO (characterized by the MgO_2^- signals). This indicates that bilayer structure remains on polished and NaOH-treated Mg metallic substrate after exposure to Cl, which is consistent with previous reports [25,40–43]. The reason of the NaOH-treated sample has thinner $Mg(OH)_2$ layer after immersion is due to the presence of a thick $Mg(OH)_2/MgO$ layer formed by the NaOH treatment limits the Mg corrosion process [44]. Finally, a CO_3^{2-} signal is detected for the two samples. It indicates the formation of $MgCO_3$ located in the outer $Mg(OH)_2$ layer. All these observations are in good agreement with the XPS results presented above. Furthermore, MgH^- and $^{25}MgH^-$ signals, characteristic of MgH_2 [45,46], show their maximum intensities at greater depths than the $MgOH^-$ and MgO_2^- signals, indicating that MgH_2 is located close to the oxide/metal interface, which is consistent with [47]. The existence of MgH_2 in the corrosion products of Mg alloys has been previously observed with different characteristic methods, including ToF-SIMS and XRD [47]. Taking into account a critical aspect of cathodic activation in CP-Mg with high level of noble metal impurities, it was shown that the predominant contribution to H_2 evolution emanates from remote cathode sites [23,48,49]. An alternative theory considers the formation of the hydrides with further dissolution leading to evolution of H_2. Cathodic polarization of CP-Mg was used to simulate the conditions of HER process. As shown in Fig. S1, high resolution XRD (synchrotron radiation source) was carried on a polished CP-Mg during the immersion in 3.5 wt% NaCl under cathodic polarization with a 5 mA/cm^2 current density. Two small MgH_2 signals are present on all XRD patterns during continuous immersion for 60 min, indicating it is

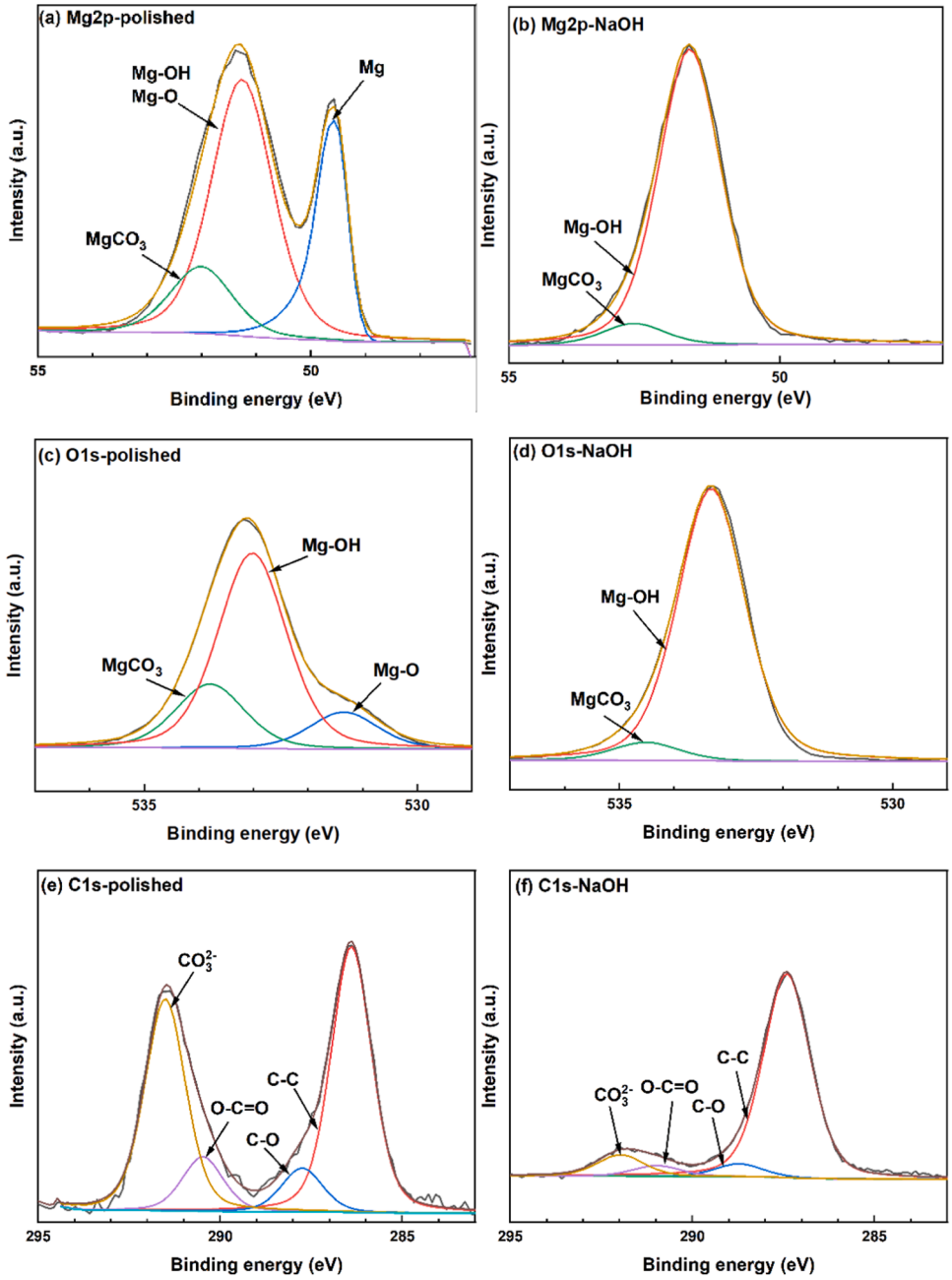

Fig. 2. XPS spectra of CP-Mg surface before corrosion immersion. Mg2p (**(a)** and **(b)**), O1s (**(c)** and **(d)**), and C1s (**(e)** and **(f)**) deconvolution spectrum of polished (**(a)**, **(c)**, and **(e)**) and NaOH-treated (**(b)**, **(d)**, and **(f)**) samples.

present among the corrosion products. Simple dissolution of MgH_2 may also be a reason of released H_2 during corrosion of Mg [49]. However, the role of MgH_2 in Mg corrosion is not the main content of this work and will not be discussed in detail in the next part.

On both samples, the stratification of the corrosion product layer, with the sequence metallic Mg/MgO/$Mg(OH)_2$, remains although the interfaces between the layers are less well defined compared to the condition before immersion. On the contrary, the $MgCO_3$ profile appears to be homogeneous throughout the layer [25,40–43].

Fig. 7 shows the ToF-SIMS negative ion depth profiles for **(a)** polished and **(b)** NaOH-treated CP-Mg samples immersed in NaCl solution containing 2,6-PDC for 15 min. The overall oxidized layer structure remains similar to what was observed previously after immersion in NaCl solution without inhibitor (Fig. 6) and $Mg(OH)_2$ and MgO are the main components in the corrosion product layer. When exposed to aggressive Cl^- containing solution with inhibitor, a marked thickening of the corrosion product layer is observed for polished Mg samples whose thickness reaches 526 nm, compared to 294 without inhibitor (see Table 5), whereas no modification of the corrosion product thickness is observed on the NaOH-treated sample (209 nm compared to 214 nm). This point will be discussed later (**Section 4.1**). According to Fig. 7, for all samples after 15 min of immersion in NaCl solution with 2,6-PDC, a very low intensity of 2,6-PDC species was found in the corrosion product layer. In Fig. 6 and Fig. 7, the Cl^- presents in the whole corrosion product layer, which is attributed to the ingress it during immersion. Remarkably, after immersion in NaCl solution with the addition of 2,6-PDC, the Cl^- intensity is reduced in the corrosion product for the two substrates, compared to substrates exposed to NaCl solution only. Moreover, the distribution of the Cl^- ions in the corrosion product is strongly affected (it is even more pronounced on the NaOH-treated substrate) after the

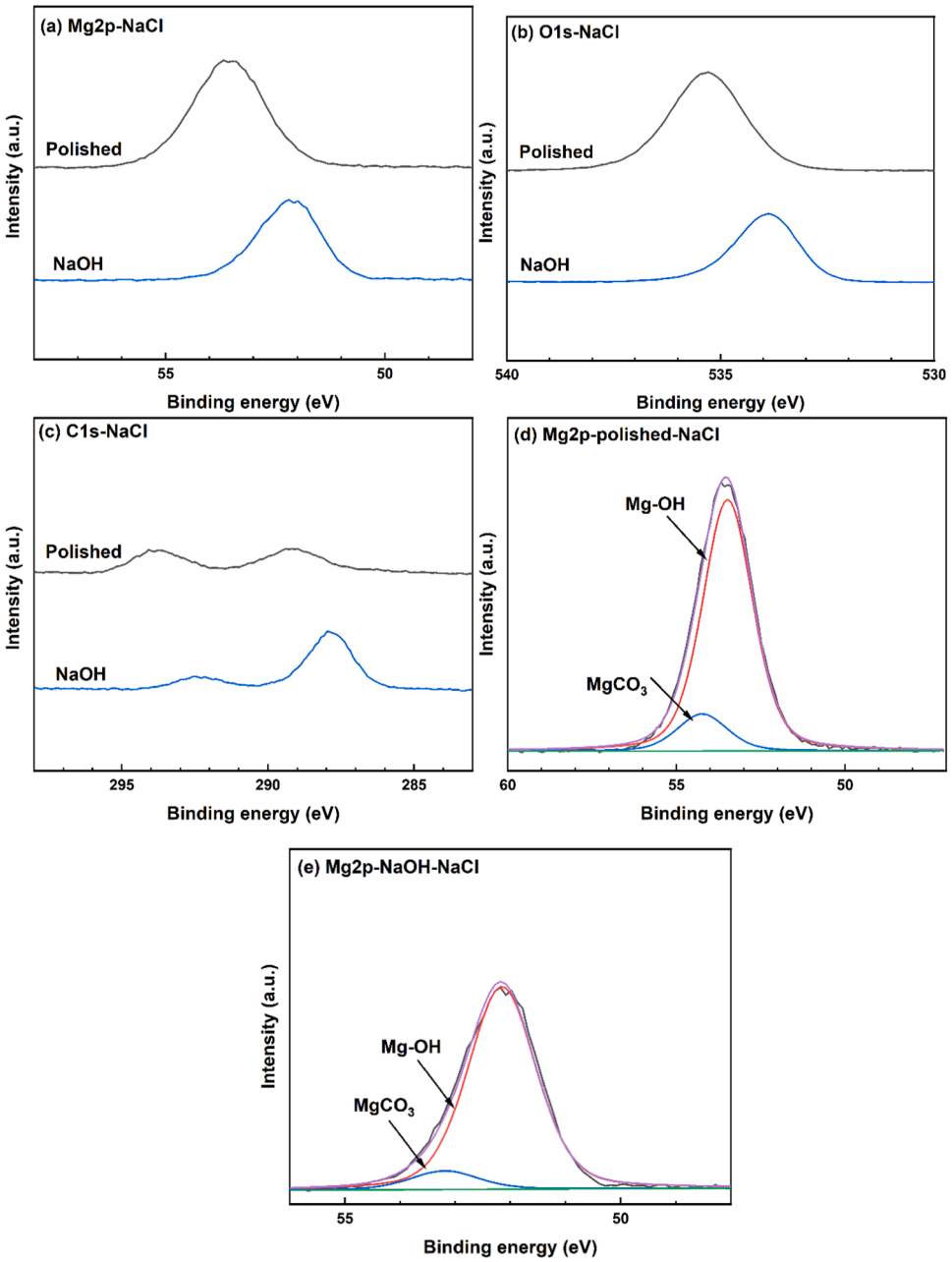

Fig. 3. XPS spectra of CP-Mg surface after 15 min corrosion immersion in NaCl **(a-c).** O1s fitted spectra for polished **(d)** and NaOH-treated **(e)** samples after 15 min of immersion in NaCl.

addition of 2,6-PDC, with a decrease of the Cl^- concentration on the external surface and in the corrosion product layer whereas the concentration remains similar to substrate exposed to the NaCl solution at the metal/oxide interface. These observations shows that the Cl^- intensity and the corresponding distribution in corrosion product was affected by 2,6-PDC. Further mechanistic details are described in **Section 4.1**.

The evolution of PDC characteristic surface peaks of $C_6H_3NO_2MgOH^-$ **(a)** and $C_7H_4NO_4MgO^-$ **(b)** and profiles of Cl^- **(c)** are presented in Fig. 8. From Fig. 8 **(a)** and **(b)**, it is clearly seen that the characteristic fragments ($C_6H_3NO_2MgOH^-$ and $C_7H_4NO_4MgO$) signals, recorded on the extreme surface, have higher intensity for the polished Mg sample than those of NaOH-treated samples, suggesting a relatively stronger reactivity towards this surface. However, these species, characteristic of the inhibitor, are only observed on the outer surface, Fig. 7, (several nanometers thick) with very low intensities in the depth profiles, indicating that they are not distributed through the corrosion product but are only adsorbed on the outer surface. Looking at the Cl^- signal (Fig. 8 **(c)**), it is obvious that after immersion in inhibitor containing solution, Cl^- normalized intensity of NaOH-treated Mg is lower compared with that of polished Mg. The lower Cl^- concentration observed on the substrate shows the lower adsorbed inhibitor concentration on the outer surface (Fig. 8 **(a)** and **(b)**). This seems indicates that there is no positive correlation between the amount of 2,6-PDC adsorbed on the surface and the Cl^- penetration. Therefore, observation of samples after a short time of exposure and systemic corrosion experiments should be carried out to explore the inhibition mechanism of 2,6-PDC.

3.3. *Surface morphology*

Fig. 9 displays the electron micrographs of polished CP-Mg surfaces, top view after being exposed to NaCl **(a)** and NaCl solution with 2,6-PDC

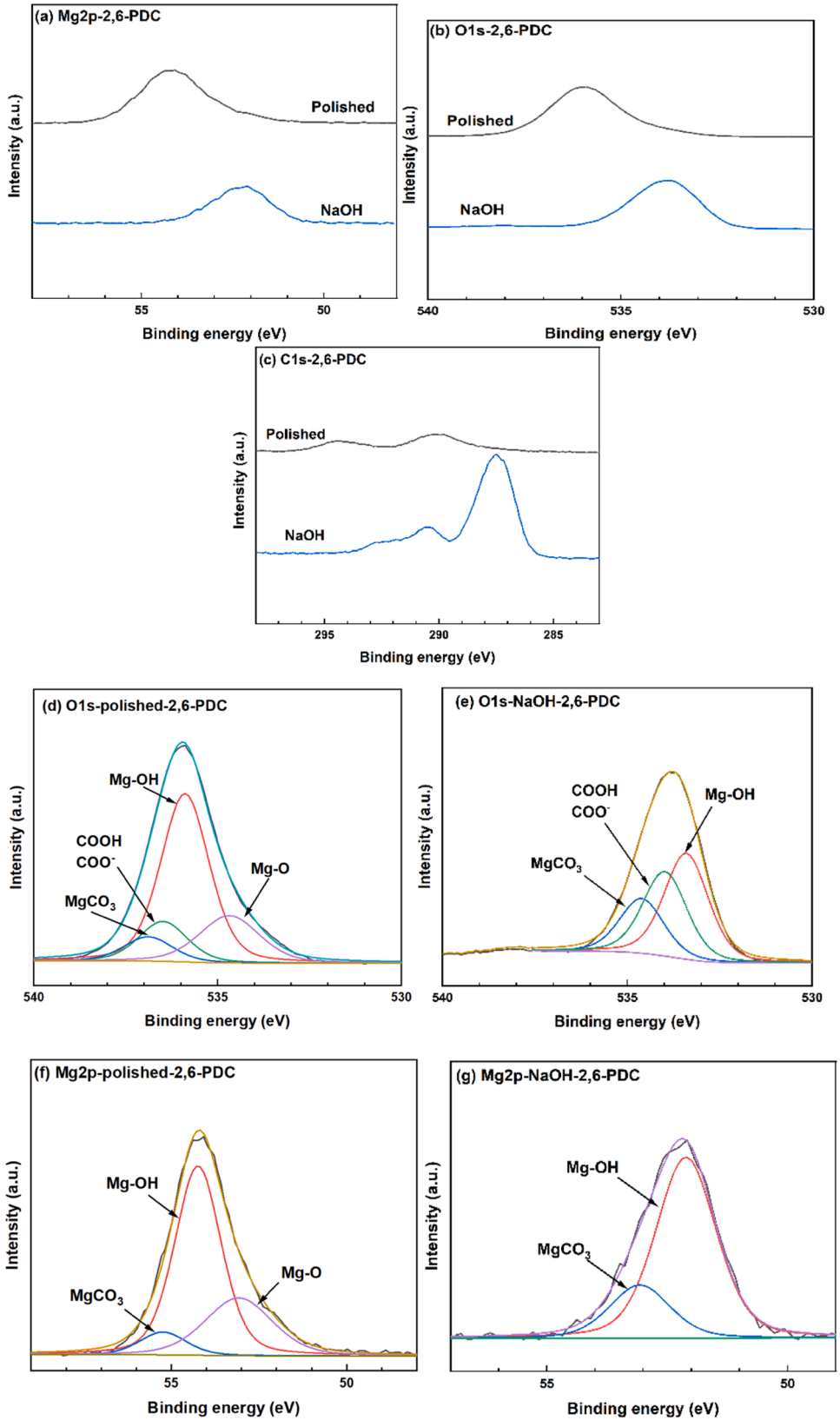

Fig. 4. XPS spectra of CP-Mg surface after 15 min immersion in NaCl with 2,6-PDC **(a-c)**. Evolution of the O1s spectra after 15 min immersion in NaCl with 2,6-PDC for polished **(d)** and NaOH-treated **(e)** Mg; Mg2p fitted spectra for polished **(f)** and NaOH-treated **(g)** samples after 15 min immersion in NaCl with 2,6-PDC solution.

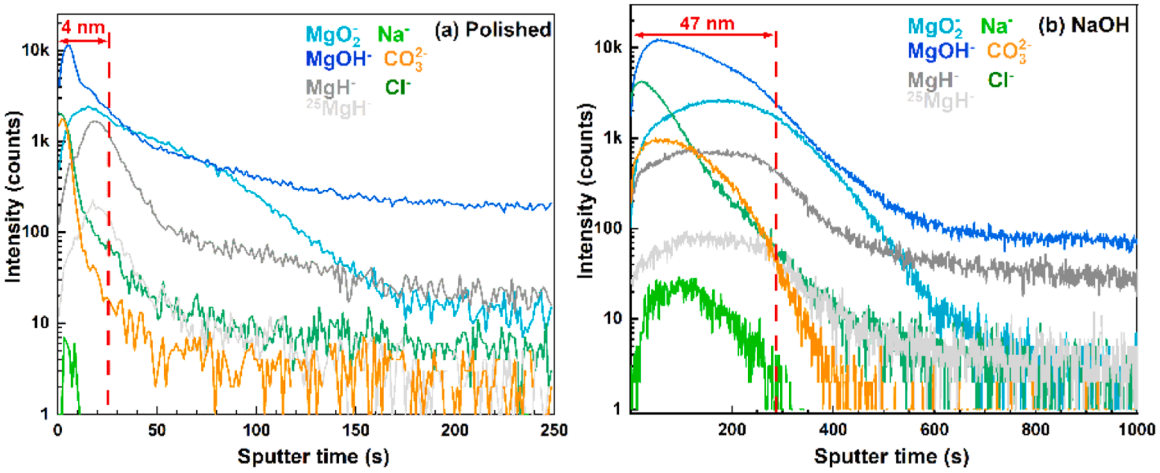

Fig. 5. As prepared surfaces of CP-Mg. ToF-SIMS (negative ions) in-depth profiles recorded on the **(a)** polished Mg and **(b)** NaOH-treated Mg surfaces.

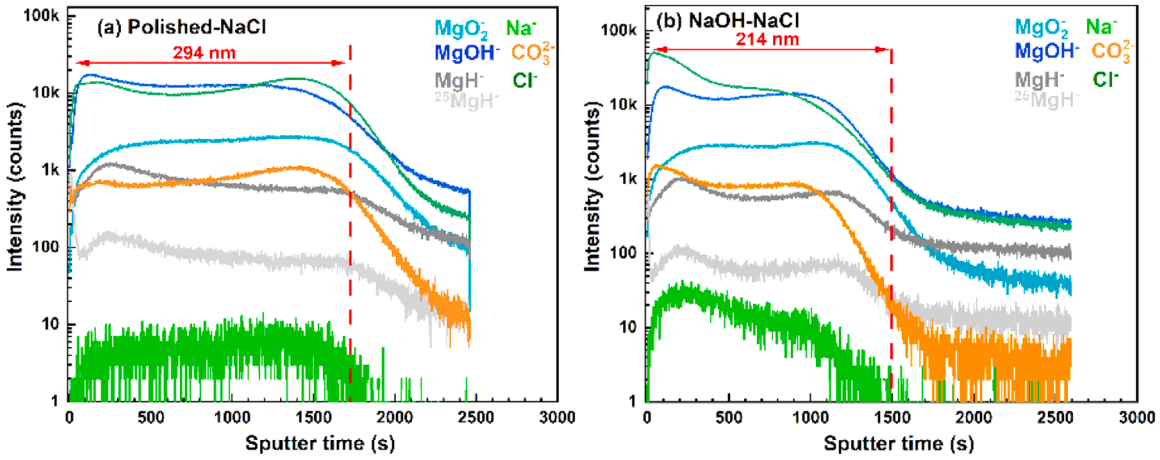

Fig. 6. CP-Mg surfaces after being exposed to NaCl solution for 15 min. ToF-SIMS negative ions in-depth profiles recorded on the **(a)** polished Mg and **(b)** NaOH-treated CP-Mg surfaces.

Table 5
Layer thickness measured by ToF-SIMS for samples with two different treatments immersed in NaCl with or without 2,6-PDC solutions for 15 min.

Layer thickness (nm)	Polished	NaOH
NaCl	294	214
NaCl+ 2,6-PDC	526	209

(b) for 30 min. Note, that high similarity of corrosion inhibition effects of 2,6-PDC and 2,5 PDC has been previously reported [5,31]. Both samples have a network-like structure consisting of different-sized sponge-like flakes. This kind of microcrystal morphology is typical for $Mg(OH)_2$ layer formed on Mg [27,50]. The samples immersed in NaCl with 2,6-PDC or 2,5-PDC display smaller size of flakes and lower porosity than those of the samples immersed in NaCl, which reduces the ingress of Cl^- and therefore provide higher corrosion resistance. This phenomenon is in line with the observation reported in [27], where denser layer of corrosion products with smaller $Mg(OH)_2$ flakes was found in presence of PDC. This is also consistent with the expected corrosion inhibition role of PDC reported in [5]. Combined with ToF-SIMS results, these observations indicate that 2,6-PDC induces a more compact corrosion product layer on CP-Mg without direct reaction with the corrosion product layer as can be concluded from very low amount of 2,6-PDC species in the corrosion product layer from Fig. 7. Fig. 9.

3.4. EIS

To investigate the CP Mg corrosion process in the absence and presence of 2,6-PDC in NaCl solution, electrochemical impedance measurements were conducted in the frequency range from 10^5 to 10^{-1} Hz. Fig. 10 presents the Bode plots of samples in NaCl solution with or without 2,6-PDC. The low-frequency impedance value at 0.1 Hz (Z_{mod} at 0.1 Hz, $|Z|_{0.1}$) reflects the overall corrosion resistance of the sample, a higher Z_{mod} at low frequency indicates better corrosion resistance [32, 51]. Values of $|Z|_{0.1}$ for all samples during 24 h of immersion are presented in Fig. 12 **(a)**. In the blank NaCl electrolyte, both samples show a rapid drop of $|Z|_{0.1}$ within the first hour of immersion. The impedance of the NaOH-treated Mg sample in NaCl solution (Fig. 10 **(c)**) is slightly higher than that of polished samples for the first 15 min. The reason is that the porous oxide/hydroxide layer grown during the NaOH treatment provides additional weak barrier [44]. From the phase angle plots, in the case of samples immersed in NaCl solution, it can be seen that there are at least two time constants at the first 15 min and only one well defined time constant after 3 h of immersion. As marked in Fig. 10, the time constant at the high frequency originates from the barrier properties of the oxide layer; the time constant at the middle frequency is attributed to the charge transfer process of Mg corrosion [42]. This means the pre-formed layer produced by both surface treatments could protect the bulk Mg at first, but the Cl^- destroyed the layer in a short time [41,42].

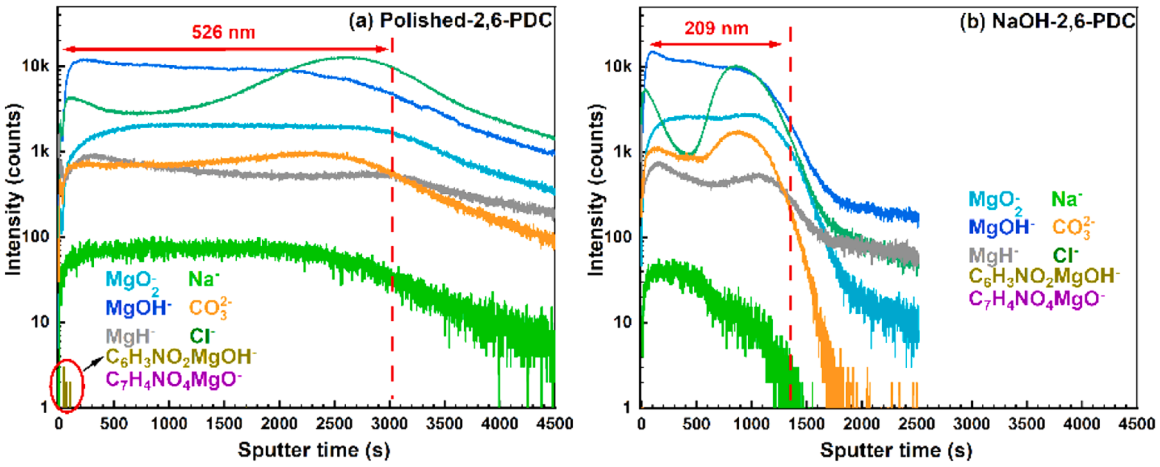

Fig. 7. CP-Mg surfaces after being exposed to NaCl solution containing 2,6-PDC for 15 min. ToF-SIMS (negative ions) in-depth profiles on the **(a)** polished Mg and **(b)** NaOH-treated CP-Mg surfaces.

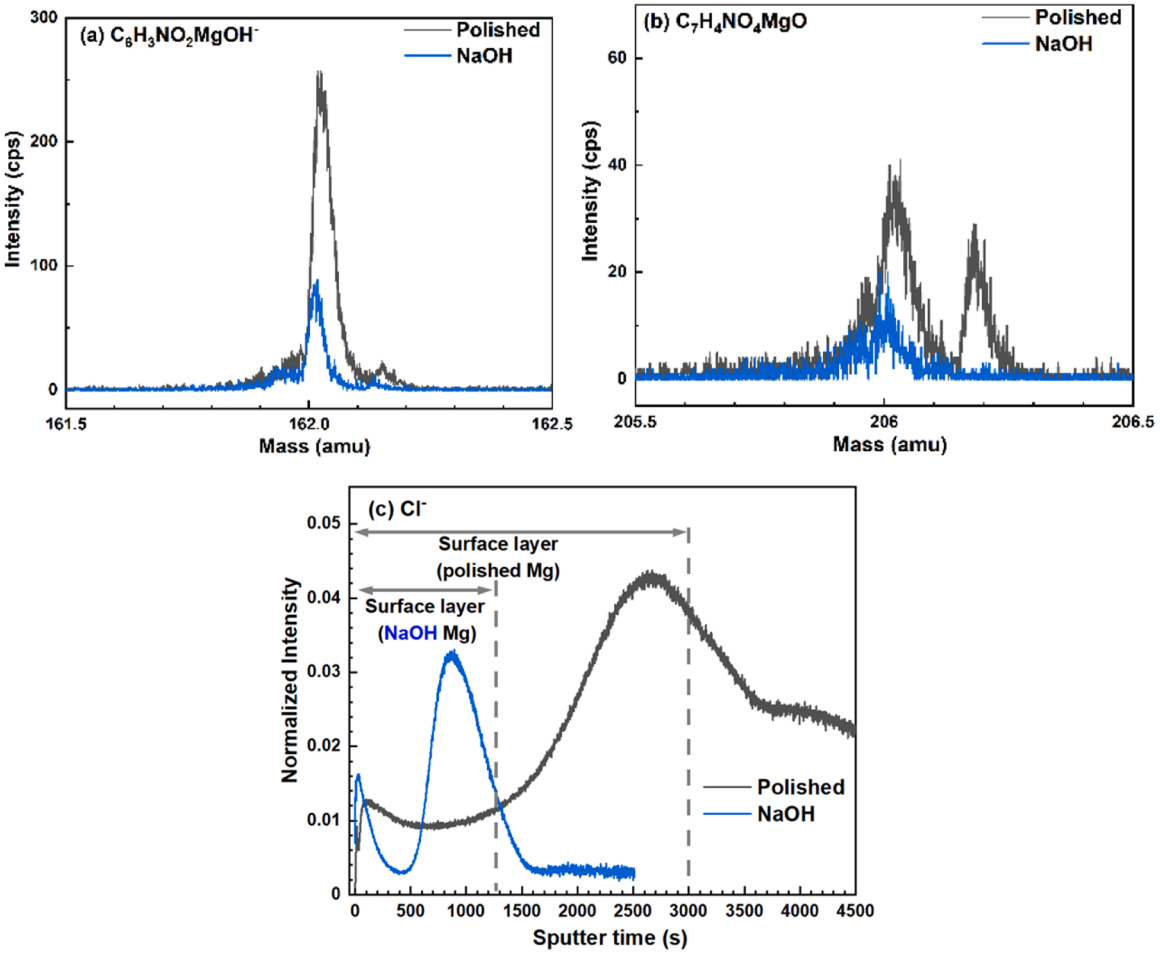

Fig. 8. Evolution of characteristic peaks in the mass spectra of 2,6-PDC at **(a)** 162.0041 amu ($C_6H_3NO_2MgOH^-$) and at **(b)** 205.9940 amu ($C_7H_4NO_4MgO$) and **(c)** profiles of Cl^- fragment obtained for polished (black) and NaOH-treated (blue) Mg samples. The signal is normalized by the sum of all signals.

With the addition of 2,6-PDC into the NaCl solution (Fig. 10 **(b)** and **(d)**, and Fig. 12 **(a)**), it is clearly seen that the Z_{mod} values of NaOH-treated sample are the highest at 15 min, indicating NaOH treatment better prevents the ingress of Cl^-, which is consistent with ToF-SIMS results (Fig. 8 **(c)**). However, corrosion resistance was lower in the first 15 min for both samples in NaCl solution with 2,6-PDC than those in the blank NaCl solution. With increasing immersion time, corrosion resistance improves noticeably and eventually achieves higher values than that in blank NaCl solution due to the formation of a denser corrosion product layer. Furthermore, their Bode plots present two time constants during whole immersion process. These phenomena confirm that 2,6-PDC increases the corrosion resistance of CP-Mg in NaCl solution over a longer immersion time, even though it decreases Mg corrosion resistance in the first 15 min.

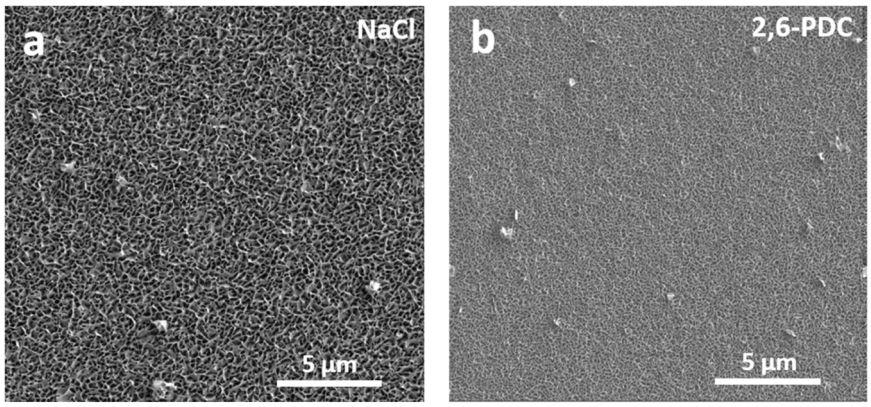

Fig. 9. SEM micrographs, top view of polished CP-Mg after 30 min of immersion in solutions of NaCl **(a)** and NaCl with 0.05 M 2,6-PDC **(b).**

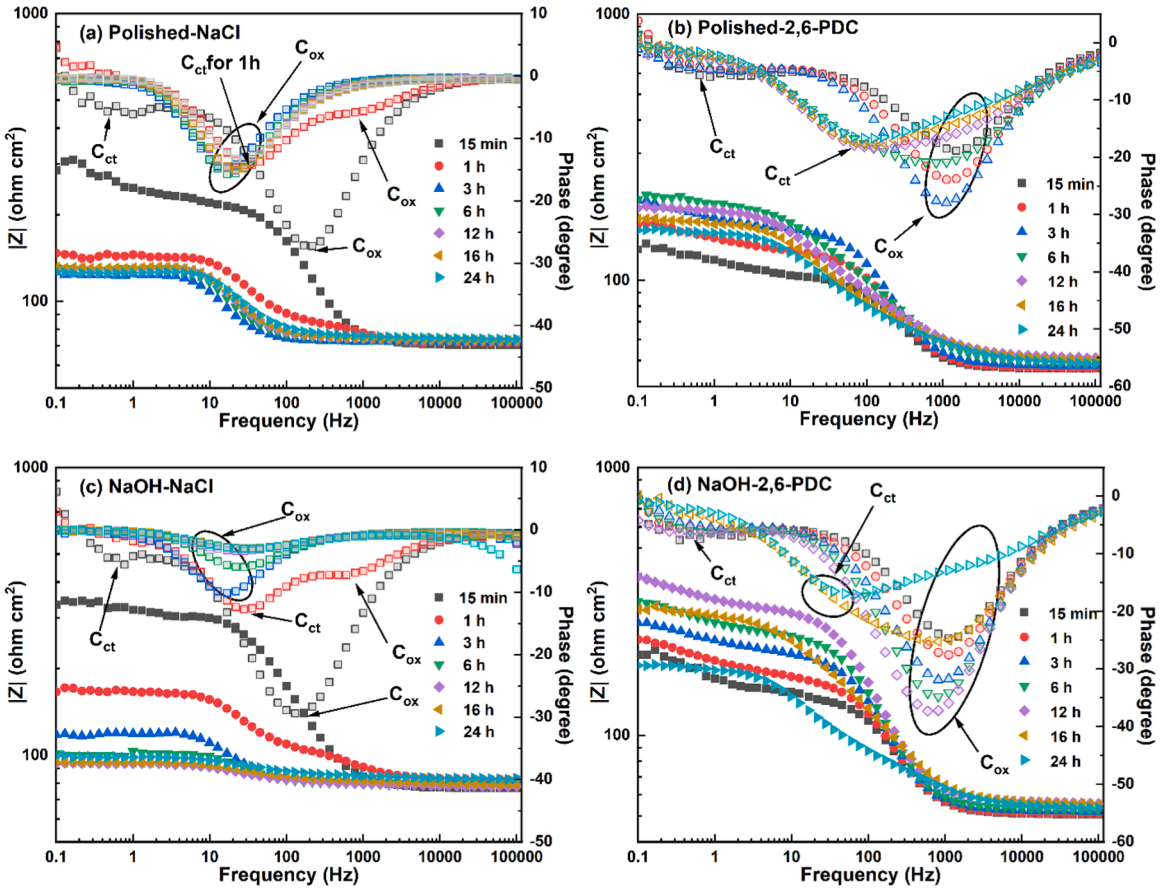

Fig. 10. Evolution of Bode plots for **(a)** polished Mg and **(c)** NaOH-treated Mg during 24 h immersion in NaCl solution; **(b)** polished Mg and **(d)** NaOH-treated Mg during 24 h immersion in NaCl with 2,6-PDC solution.

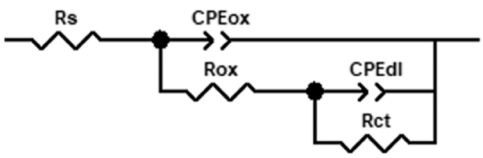

Fig. 11. Equivalent circuits with two time constants.

In the case of NaCl solution with 2,6-PDC for polished sample (Fig. 10 **(b)**, and Fig. 12 **(a)**), after the initial increase for the first 6 h of immersion, $|Z|_{0.1}$ shows a gradual decrease till the end of 24 h, suggesting there is a penetration of the corrosive electrolyte or partial breakdown of the formed corrosion product layer. The impedance of the NaOH-treated sample in NaCl solution with 2,6-PDC (Fig. 10 **(d)**) increases and then decreases after around 12 h. Thus, all these phenomena suggest the NaOH treatment further enhances the inhibition effect of 2,6-PDC.

In order to quantitatively analyze the corroding system, the impedance plots were fitted with equivalent electrical circuits as presented in Fig. 11. The fitted results of Bode plots presented in Fig. 10 are listed in Table 6 and R_{ox} values for all samples (EIS results of some parallel samples are not presented here) are also presented in Fig. 12 **(b)**. R_s indicates the solution resistance; R_{ox} denotes the resistance of the oxide

Table 6
Fit circuit values for polished ((**a**) and (**b**)) and NaOH-treated ((**c**) and (**d**)) samples, in NaCl solution ((**a**) and (**c**)) or NaCl with 2,6-PDC ((**b**) and (**d**)) solution (Bode plots for all samples are presented in Fig. 10).

(**a**) Polished-NaCl	Rs (Ω cm^2)	CPE_{ox} T_1 (Ω^{-1} cm^{-2} s$^{-\alpha}$)	P	R_{ox} (Ω cm^2)	CPE_{dl} T_1 (Ω^{-1} cm^{-2} s$^{-\alpha}$)	P	R_{ct} (Ω cm^2)
15 min	70.24	1.89×10^{-5}	0.90	153.50	4.38×10^{-3}	0.79	78.72
1 h	71.52	2.87×10^{-5}	0.91	18.60	1.13×10^{-4}	0.97	54.10
3 h	72.85	2.53×10^{-4}	0.98	51.83			
6 h	74.11	2.04×10^{-4}	0.98	58.05			
12 h	74.72	1.83×10^{-4}	0.97	57.44			
16 h	74.70	1.91×10^{-4}	0.95	58.60			
24 h	75.71	1.98×10^{-4}	0.93	52.59			

(**b**) Polished-2,6-PDC	Rs (Ω cm^2)	CPE_{ox} T_1 (Ω^{-1} cm^{-2} s$^{-\alpha}$)	P	R_{ox} (Ω cm^2)	CPE_{dl} T_1 (Ω^{-1} cm^{-2} s$^{-\alpha}$)	P	R_{ct} (Ω cm^2)
15 min	46.47	3.45×10^{-5}	0.89	55.94	9.61×10^{-3}	0.65	37.20
1 h	46.73	2.98×10^{-5}	0.89	82.69	7.55×10^{-3}	0.78	32.95
3 h	47.79	2.61×10^{-5}	0.90	109.90	8.77×10^{-3}	0.76	42.10
6 h	49.17	5.45×10^{-5}	0.80	77.97	4.31×10^{-4}	0.72	73.69
12 h	50.84	1.36×10^{-4}	0.70	75.46	2.00×10^{-4}	0.88	62.59
16 h	49.86	1.81×10^{-4}	0.68	63.70	1.49×10^{-4}	0.93	56.37
24 h	48.60	1.78×10^{-4}	0.67	44.12	1.89×10^{-4}	0.85	63.06

(**c**) NaOH-NaCl	Rs (Ω cm^2)	CPE_{ox} T_1 (Ω^{-1} cm^{-2} s$^{-\alpha}$)	P	R_{ox} (Ω cm^2)	CPE_{dl} T_1 (Ω^{-1} cm^{-2} s$^{-\alpha}$)	P	R_{ct} (Ω cm^2)
15 min	76.23	2.83×10^{-5}	0.85	237.50	7.21×10^{-3}	1.04	34.55
1 h	82.18	3.97×10^{-5}	0.84	30.79	1.20×10^{-4}	0.99	53.42
3 h	83.41	3.32×10^{-4}	0.96	37.98			
6 h	80.09	4.23×10^{-4}	0.93	21.99			
12 h	79.39	1.40×10^{-4}	0.75	15.27			
16 h	81.21	1.51×10^{-3}	0.72	14.28			
24 h	84.23	1.51×10^{-3}	0.71	15.32			

(**d**) NaOH-2,6-PDC	Rs (Ω cm^2)	CPE_{ox} T_1 (Ω^{-1} cm^{-2} s$^{-\alpha}$)	P	R_{ox} (Ω cm^2)	CPE_{dl} T_1 (Ω^{-1} cm^{-2} s$^{-\alpha}$)	P	R_{ct} (Ω cm^2)
15 min	50.56	2.56×10^{-5}	0.90	91.54	6.52×10^{-3}	0.71	71.45
1 h	50.90	2.35×10^{-5}	0.91	110.80	6.49×10^{-3}	0.61	77.58
3 h	51.91	2.24×10^{-5}	0.91	151.90	5.45×10^{-3}	0.75	61.39
6 h	52.72	2.16×10^{-5}	0.90	187.80	4.97×10^{-3}	0.78	80.05
12 h	56.13	2.11×10^{-5}	0.90	241.90	5.58×10^{-3}	0.74	113.70
16 h	55.41	3.43×10^{-5}	0.83	108.10	3.34×10^{-4}	0.68	132.70
24 h	53.36	1.41×10^{-4}	0.69	53.02	2.53×10^{-4}	0.85	76.19

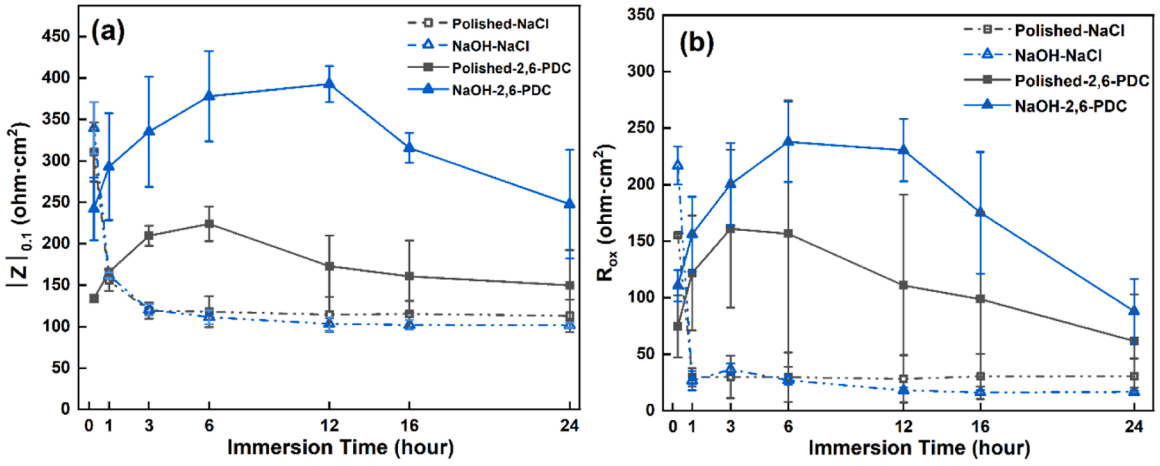

Fig. 12. $|Z|_{0.1}$ at 0.1 Hz **(a)** of two kinds of samples immersed in NaCl with or without 2,6-PDC solutions for 24 h; and R_{ox} **(b)** values of two kinds of samples immersed in NaCl with 2,6-PDC solution for 24 h.

layer on the Mg surface, and CPE_{ox} is a constant phase element describing the capacitive behavior of the oxide layer; R_{ct} is coupled with the CPE_{dl} to model the charge transfer resistance and the constant phase element for the double-layer, respectively. In terms of R_{ox} (oxide layer resistance), both samples in NaCl solution with 2,6-PDC addition have lower values than the sample in blank NaCl solution in the first 15 min.

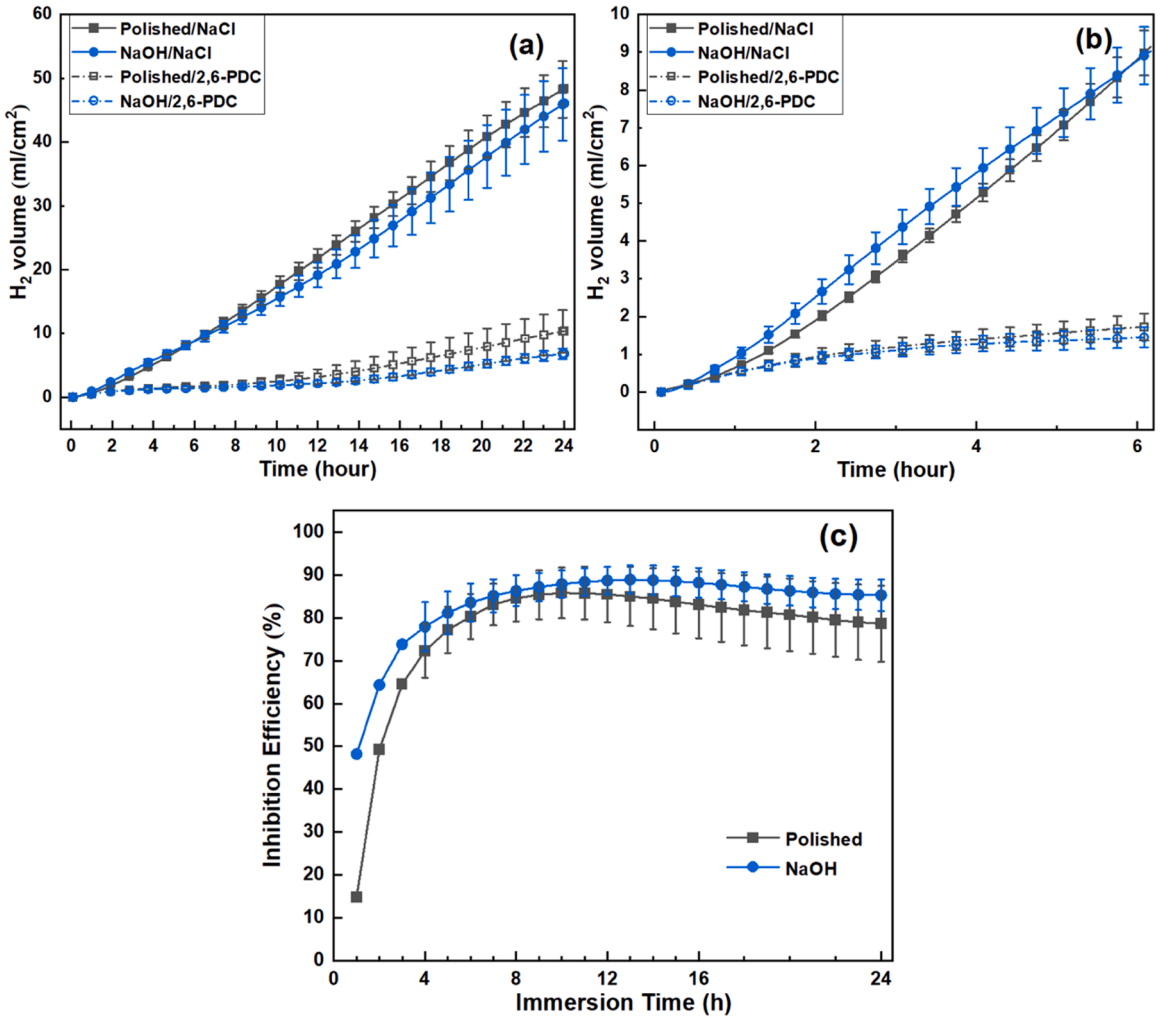

Fig. 13. H_2 evolution results for two types of samples in NaCl with or without 2,6-PDC solutions for 24 h **(a)** and the zoom into the initial 6 h **(b)**; inhibition efficiency of 2,6-PDC for two samples in different immersion time calculated based on the hydrogen evolution values **(c)**.

From Fig. 12 **(b)**, when immersed for a longer time, in the case of polished samples in the NaCl solution containing 2,6-PDC, oxide layer resistance increases to about 150 Ω cm^2, after longer immersion polished Mg sample shows a gradual decrease in $R_{ox,}$ to about 50 Ω cm^2 at 24 h. For the NaOH-treated sample, the oxide layer resistance reaches values above 230 Ω cm^2 after 6-hour immersion and maintains this value after 12-hour immersion, which is higher than polished Mg samples, revealing the stronger barrier properties and stability of NaOH-treated sample in NaCl solution with 2,6-PDC.

Therefore, when 2,6-PDC is present in the electrolyte, it reduces the resistance of the oxide layer at the initial stage, due to the slight dissolution of $Mg/MgO/Mg(OH)_2$. However, after some time of immersion, the oxide resistance increases, indicating that the presence of 2,6-PDC stabilizes the oxide layer, likely by promoting the formation of a more protective layer of corrosion product, which prevents oxide from being easily disturbed or affected by corrosive electrolyte. When samples are immersed for a longer time, the protective layer of corrosion products is partially eroded by Cl^-.

3.5. Hydrogen evolution

Fig. 13 shows the hydrogen evolution results for both treated samples immersed in NaCl solution with or without 2,6-PDC. Also, the inhibition efficiencies of 2,6-PDC after both surface treatments, based on H_2 evolution at different immersion times, are shown in Fig. 13 **(c)**. From Fig. 13 **(c)**, it is found that the IE of 2,6-PDC for NaOH-treated samples is marginally higher, demonstrating low influence of NaOH treatment on the IE of 2,6-PDC. Also, it could be found that the inhibition effect of 2,6-PDC on both samples increases rapidly within the first 8 h, this process is the activation of the inhibitor and development of a protection conversion layer. After about 10 h, a performance plateau is reached, and the maximum inhibition efficiency has been reached (86% for polished sample at 11th hour, 89% for NaOH-treated sample at 13th hour). Therefore, the NaOH treatment slightly improves the inhibition effect of 2,6-PDC on Mg surface.

3.6. Local concentration of dissolved oxygen and hydrogen by microprobes

To better understand the rapid evolution of localized behavior, evolution of concentration of dissolved molecular hydrogen and oxygen was recorded locally, 50 μm above the surface of CP-Mg samples surface in two electrolytes: NaCl and that with 2,6-PDC. Fig. 14 presents the change of local concentrations of DH and DO (measured 50 μm from the active surface) during the first 6 h. It emerged recently [52–56] that the cathodic process during Mg corrosion is supported by two cathodic pathways: hydrogen evolution reaction (HER) and oxygen reduction reaction (ORR). The reactions are shown in Eq. (8) and Eq. (9).

In NaCl solution, the DH concentration of NaOH-treated sample has lower value during the entire course of immersion due to the pre-formed

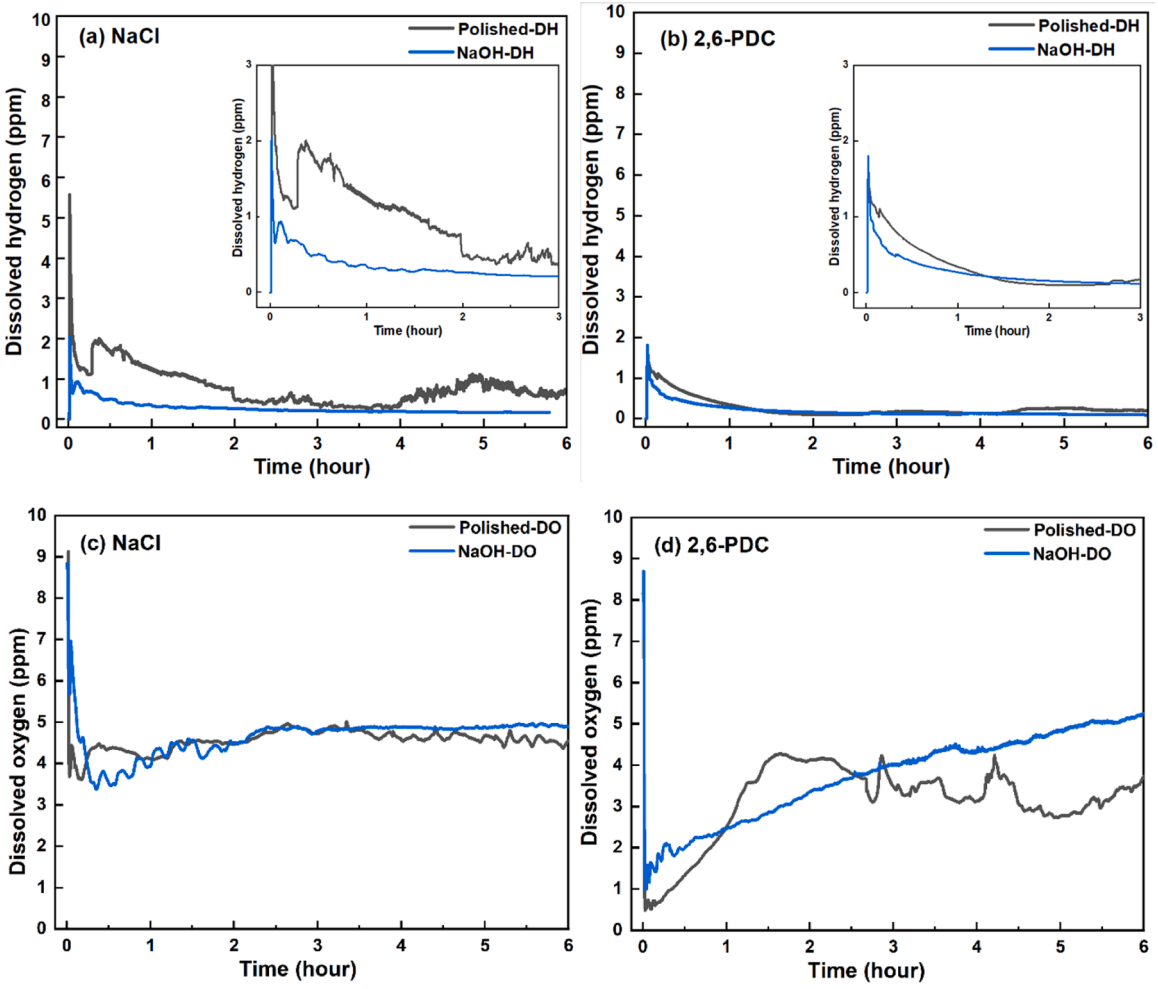

Fig. 14. Evolution of the local concentration of dissolved molecular hydrogen **(a)**, **(b)** and dissolved oxygen **(c)**, **(d)** 50 μm above the surface of CP-Mg samples immersed either in NaCl solution **(a)** and **(c)** or; 2,6-PDC + NaCl solution **(b)** and **(d)**.

$Mg(OH)_2$/MgO layer on Mg surface (Fig. 14 **(a)**). With the addition of 2,6-PDC, the hydrogen evolution decreased. This difference is especially pronounced during the first hour of immersion for polished sample, consistent with ToF-SIMS finding that the thickness of the surface layer for polished sample is higher in NaCl 2,6-PDC-containing solution than that in NaCl solution. The DO concentration in NaCl 2,6-PDC-containing solution (0.5 ppm for polished and 2 ppm for NaOH sample) is obviously lower compared to that in NaCl solution during the first 15 min. This suggests that the initially formed MgO/$Mg(OH)_2$ layer (concluded from Fig. 7) during immersion is influenced by 2,6-PDC: 2,6-PDC promotes formation of a oxide/hydroxide layer that requires initial surface activation, exposing Mg surface to free oxygen access. Besides, the formation of this kind of oxide/hydroxide layer will consume more O_2 than that in NaCl solution. Owing to the pre-formed MgO/$Mg(OH)_2$ layer on NaOH-treated samples, the ORR is slightly lower and the concentration of remaining dissolved oxygen is slightly higher than for polished sample during the first hour. This is consistent with the previous report that thicker layer of $Mg(OH)_2$ hinders oxygen diffusion to and reduction at Mg surface [52]. When the immersion is longer, the pre-formed MgO/$Mg(OH)_2$ layer on NaOH-treated sample is partly dissolved by 2,6-PDC and no longer hinders the diffusion of 2,6-PDC enabling formation of denser and more protective oxide/hydroxide layer and lower DO concentration from 1 h to about 2.5 h. Since the NaOH-treated sample had formed an oxide/hydroxide layer with higher barrier properties after 2.5 h, the ORR reaction could be better blocked, and the DO concentration returned to higher level of the two differently treated samples.

$$\text{HER}: 2H_2O + 2e^- \rightarrow \quad H_2\uparrow + 2OH^- \tag{8}$$

$$\text{ORR}: \quad O_2 + 4e^- + 2H_2O \quad \rightarrow 4OH^- \tag{9}$$

4. Discussion

According to the EIS results, the impedance values of samples in 2,6-PDC-containing solutions are lower than those in NaCl solution for the first 15 min; after that, they are higher in NaCl solution with 2,6-PDC than those in NaCl solution (Fig. 10 and Fig. 12 **(b)**). In Fig. 6 and Fig. 7, ToF-SIMS profiles show that with the increase of corrosion product layer thickness after the addition of 2,6-PDC, the depth of Cl^- penetration also increases for polished sample while the intensities of Cl^- for both samples decrease during this stage. The intensity of Cl^- for NaOH-treated sample immersed in NaCl solution with 2,6-PDC decreases first and then increases to a peak value and decreases again from the surface to the interior while it keeps decreasing after being immersed in NaCl solution. These observations suggest that this period of corrosion process in NaCl solution with 2,6-PDC is dominated by 2,6-PDC, which is different from that in NaCl solution. Furthermore, the local concentration of dissolved hydrogen and especially dissolved oxygen in NaCl solution with 2,6-PDC is lower than that in blank NaCl solution, especially at the beginning of corrosion, Fig. 14. While the corrosion rate with or without 2,6-PDC is the same for the 15 min of immersion (Fig. 13), lower concentration of remaining O_2 and lower concentration of generated H_2 evidence stronger contribution of ORR to the total

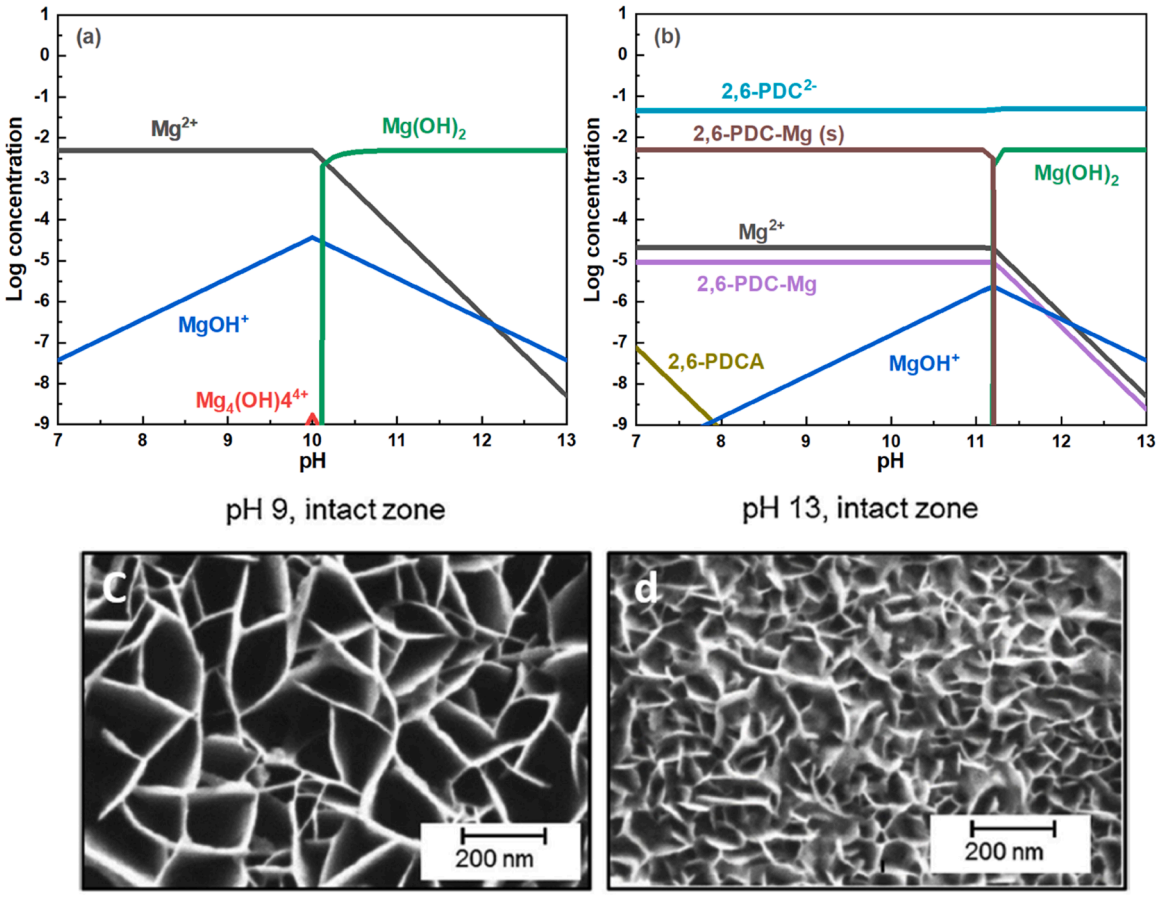

Fig. 15. Specie predominance diagram in NaCl aqueous electrolyte **(a)** without and **(b)** with 2,6-PDC^{2-}made using Hydra-Medusa. Input ions and their equilibrium concentrations: Mg^{2+}(5 mM), Na^{+} (58.5 mM) Cl^{-} (8.5 mM), and 2,6-PDC^{2-}(50 mM). The stability constant of 2,6-PDC with Mg^{2+} was found in [29] and added manually to Hydra-Medusa database, the solubility product of 2,6-PDC-Mg was replaced by that of $MgCO_3$ because there are no relevant parameters in the current database; typical ex-situ SEM micrograph of the Mg surface after 2 h of immersion in 0.1 M NaCl solution with different pH: 9 **(c)** and 13 **(d)**.
C) and d) were originally published by Maltseva et al. [57] and shown here for demonstration and reproduced with permission from Elsevier [57].

cathodic process on Mg in presence of 2,6-PDC. 2,6-PDC increases the ORR rate during the activation stage, and the conversion layer with MgO/$Mg(OH)_2$ forms on the surface consuming a large amount of O_2 during the first 30 min. Therefore, at the beginning of corrosion process, 2,6-PDC forms soluble complexes with Mg^{2+}, resulting in lower corrosion resistance (evidenced by EIS results at the first minutes), so the very initial interaction of 2,6-PDC with the Mg surface decreases the thickness of the $Mg(OH)_2$ layer. Thus, O_2 can easily diffuse towards the Mg substrate and participate in ORR, which reflects the high initial consumption of O_2 in the presence of 2,6-PDC. Formation of complexes of Mg with 2,6-PDC has been recently demonstrated by our group [31].

To better explain the inhibition mechanism of 2,6-PDC, the species predominance diagram, calculated using thermodynamic stability constants is presented in Fig. 15**.** It shows chemical equilibria in NaCl aqueous electrolyte **(a)** without and **(b)** with 2,6-PDC. Addition of 2,6-PDC into the NaCl solution in contact with Mg substrate leads to formation of soluble 2,6-PDC-Mg complexes ($\log k^{st}_{Mg^{2+}} = 2.7$ [29]). This decreases the concentration of free Mg^{2+} ions. Therefore, taking into account that the solubility product is constant, the pH required to form $Mg(OH)_2$ increases. Corrosion of the Mg surface leads to higher local pH. When sufficiently high concentration of OH^{-} is reached, 2,6-PDC-Mg complex and free Mg^{2+} converts to $Mg(OH)_2$, Fig. 15 **(a)** and **(b)**. It has been previously shown by Maltseva, et al. [57], that higher pH favors the formation of smaller flakes of $Mg(OH)_2$ Fig. 15 **(c)** and **(d)**. This is also in line with the cross-section SEM images in Fig. S2 ***(a)*** and ***(b)*** showing that denser Mg oxide/hydroxide layer is formed in presence of PDC with better barrier properties, thereby preventing further O_2 penetration towards the Mg substrate. Given that the NaOH-treated sample has a pre-formed $Mg(OH)_2$ layer, it should be difficult to form a oxide/hydroxide layer as thick as that on polished sample in a short time; this could explain why the thickness of the corrosion product layer on the NaOH-treated sample barely changed in both solutions.

Overall, from ToF-SIMS, EIS, and the local DO concentration results, it could be inferred that ORR rate is high during the first hour of immersion and promotes formation of dense $Mg(OH)_2$/MgO layer in presence of 2,6-PDC. The formed layer in turn improves the corrosion resistance of CP-Mg. The presence of MgH^{-} in ToF-SIMS in-depth profiles indicates MgH_2 is actually formed during the corrosion process.

According to XPS and ToF-SIMS results, there is no significant adsorption of 2,6-PDC either on as polished or NaOH-treated sample surface. NaOH-treated sample has thicker (47 nm) corrosion product layer. It has been reported that the hydroxyl groups could facilitate the adsorption of carboxylates [27,28,58–60]. However, according to the ToF-SIMS results, Fig. 8 **(a)** and **(b)**, Mg-2,6-PDC characteristic peaks intensities are overall weak, yet distinguishable: two times higher for polished surface compared to NaOH-treated. In the present study, the local pH above the sample during corrosion should be below 12 [54] and $Mg(OH)_2$ should be positively charged when the solution pH is below 12 [28,61–63]. This results in the interaction between negatively charged 2,6-PDC and the sample surface by electrostatic attraction. However, for NaOH-treated samples, the thicker and porous pre-formed MgO/$Mg(OH)_2$ layer provides higher amount of nucleation sites for the formation of $Mg(OH)_2$ compared to polished sample. Therefore, it is expected that corrosion product layer formed on NaOH-treated sample is denser and

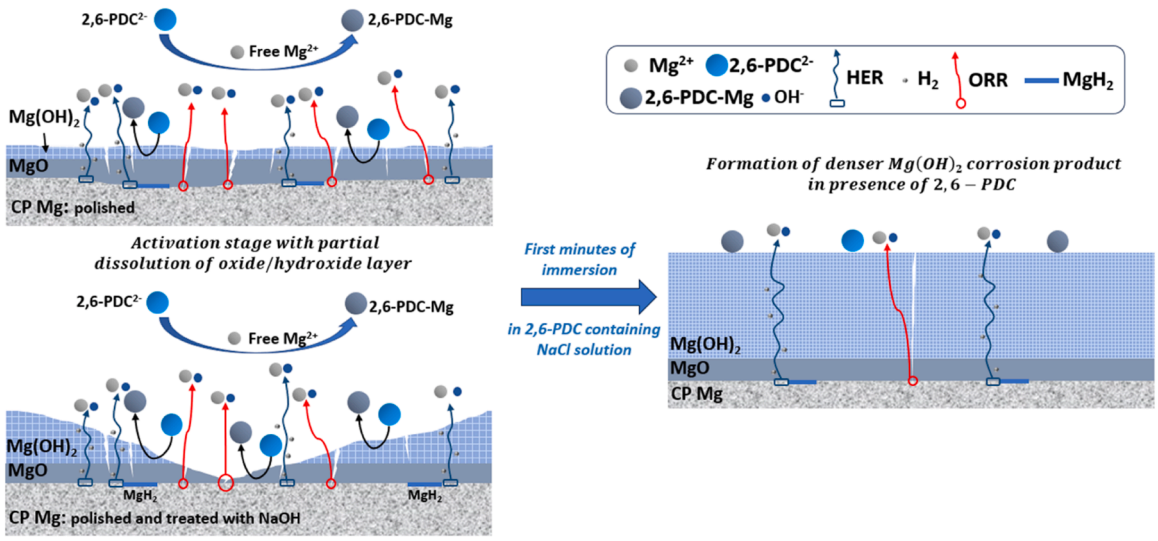

Fig. 16. The schematic representation of the inhibition mechanism of 2,6-PDC on CP-Mg.

therefore slightly improves the inhibition effect of 2,6-PDC on Mg. Furthermore, the comparison of the intensity of Cl^- signals in Fig. 6, Fig. 7, and Fig. 8 **(c)** revealed that the addition of 2,6-PDC induces a stronger change in the corrosion process for NaOH-treated samples than polished sample because only NaOH-treated sample has a very different distribution after immersion in NaCl solution with 2,6-PDC compared to NaCl solution.

Considering the experimental study on corrosion inhibition behaviors and molecular features of 2,6-PDC, the feasible inhibition mechanism can be described as shown in Fig. 16.

In this study, as shown in Fig. 16, the pre-formed MgO/$Mg(OH)_2$ layer is partially dissolved in presence of 2,6-PDC due to Mg-2,6-PDC complex formation. This is the reason for the corrosion resistance of CP-Mg in 2,6-PDC containing NaCl solution being lower than that in NaCl solution during the first 15 min, the activation stage. After the original MgO/$Mg(OH)_2$ layer is slightly etched by 2,6-PDC, O_2 diffuses to the bare Mg/MgO interface for ORR, which provides OH^- needed to form $Mg(OH)_2$ and more protective oxide/hydroxide layer is formed. Once the more protective oxide/hydroxide layer is formed, the diffusion of oxygen is hindered, leading to the suppression of ORR. As a result, the local concentration of DO gradually reverts to the initial concentration in the bulk electrolyte, as shown in Fig. 14 (d). Furthermore, the formation of the more protective oxide/hydroxide layer, impedes the ingress of Cl-. Smaller flakes of $Mg(OH)_2$ form denser, more protective layer in 2,6-PDC-containing NaCl solution, compared to that in pure NaCl as shown in Fig. 9, Fig. S2, Figs. 10 and 12–14. This explanation is also in line with previous report that 2,6-PDC displayed a universal inhibition effect for high and low purity Mg and a number of Mg alloys. This is also in line with previous reports by Yang et al. [13] and Maltseva et al. [27] who found that carboxylate inhibitors induced a denser oxide/hydroxide layer on Mg.

5. Conclusions

In this study, the effect of the corrosion inhibitor 2,6-PDC (50 mM) on pure magnesium exposed to 0.5 wt% NaCl was investigated. Two surface preparation routes, polishing and NaOH treatment were applied to gain a better understanding of the influence of Mg surface condition on the corrosion inhibition by 2,6-PDC.

- From XPS, ToF-SIMS, SEM, EIS and measurements of local concentrations of dissolved hydrogen and oxygen, it is found that 50 mM of 2,6-PDC promotes the formation of a denser $Mg(OH)_2$/MgO layer, which reduces the ingress of Cl^- and increases the corrosion resistance of magnesium. Only limited amount of 2,6-PDC was detected in the outer part of $Mg(OH)_2$ layer by ToF-SIMS, suggesting non-adsorption corrosion inhibition mechanism.

- The corrosion mechanism proposed includes formation of soluble weak complexes 2,6-PDC-Mg that lower the concentration of free Mg^{2+} available for formation of $Mg(OH)_2$ and delay the formation of $Mg(OH)_2$ on the pH scale. This leads to growth of smaller $Mg(OH)_2$ platelets that are more densely packed, and hence form more protective layer.

- Hydrogen evolution, SEM and EIS results show that the corrosion inhibition efficiency of 2,6-PDC is slightly improved by NaOH treatment of pure magnesium. Even though the formed layer of $Mg(OH)_2$/MgO is two times thinner, it is more corrosion resistant (as judged by higher values of R_{ox} and low frequency impedance modulus) and impedes the Cl^- ingress more effectively during the corrosion process, as shown by ToF-SIMS.

CRediT authorship contribution statement

Song Ci: Conceptualization, Investigation, Validation, Writing – original draft, Writing – review & editing. **Wang Cheng:** Investigation, Writing – review & editing. **Seyeux Antoine:** Investigation, Writing – review & editing. **Snihirova Darya:** Investigation, Writing – review & editing. **Mercier Dimitri:** Investigation, Writing – review & editing. **Vaghenfinazari Bahram:** Investigation, Writing – review & editing. **Zheludkevich Mikhail:** Supervision, Writing – review & editing, Conceptualization. **Lamaka Sviatlana:** Conceptualization, Supervision, Writing – review & editing. **Wieland Florian:** Investigation, Writing – review & editing. **Marcus Philippe:** Supervision, Writing – review & editing.

Declaration of Competing Interest

The authors declare that they have no known competing financial interests or personal relationships that could have appeared to influence the work reported in this paper.

Data Availability

The raw/processed data required to reproduce these findings cannot be shared at this time as the data also forms part of an ongoing study.

Acknowledgements

The authors would like to acknowledge the technical support from Mr. Ulrich Burmester, Mr. Volker Heitmann and Mr. Gert Wiese. Dr. Di Mei is acknowledged for preparing a set of polished CP-Mg samples for XPS and ToF-SIMS measurements. Mr. Ci Song and Dr. Cheng Wang thank China Scholarship Council for the award of fellowship and funding (No. 202008410217, 201806310128).

Appendix A. Supporting information

Supplementary data associated with this article can be found in the online version at doi:10.1016/j.corsci.2024.111867.

References

[1] M. Esmaily, J.E. Svensson, S. Fajardo, N. Birbilis, G.S. Frankel, S. Virtanen, R. Arrabal, S. Thomas, L.G. Johansson, Fundamentals and advances in magnesium alloy corrosion, Prog. Mater. Sci. 89 (2017) 92–193.
[2] H. Hornberger, S. Virtanen, A.R. Boccaccini, Biomedical coatings on magnesium alloys - a review, Acta Biomater. 8 (2012) 2442–2455.
[3] Y.F. Zheng, X.N. Gu, F. Witte, Biodegrad. Met., Mater. Sci. Eng.: R: Rep. 77 (2014) 1–34.
[4] G.L. Song, A. Atrens, Corrosion mechanisms of magnesium alloys, Adv. Eng. Mater. 1 (1999) 11–33.
[5] S.V. Lamaka, B. Vaghefinazari, D. Mei, R.P. Petrauskas, D. Höche, M. L. Zheludkevich, Comprehensive screening of Mg corrosion inhibitors, Corros. Sci. 128 (2017) 224–240.
[6] R.-G. Hu, S. Zhang, J.-F. Bu, C.-J. Lin, G.-L. Song, Recent progress in corrosion protection of magnesium alloys by organic coatings, Prog. Org. Coat. 73 (2012) 129–141.
[7] D. Zhang, F. Peng, X. Liu, Protection of magnesium alloys: from physical barrier coating to smart self-healing coating, J. Alloy. Compd. 853 (2021).
[8] X.P. Guo, G.L. Song, J.Y. Hu, D.B. Huang, Corrosion inhibition of magnesium (Mg) alloys, : Corros. Prev. Magnes. Alloy. (2013) 61–84.
[9] L. Ma, W. Li, S. Zhu, L. Wang, S. Guan, Corrosion inhibition of Schiff bases for Mg-Zn-Y-Nd alloy in normal saline: experimental and theoretical investigations, Corros. Sci. 184 (2021).
[10] Organic corrosion inhibitors: where are we now? A review. Part III. Passivation and the role of the chemical structure of organophosphates, International Journal of Corrosion and Scale Inhibition, 6 (2017).
[11] C. Monticelli, Corrosion Inhibitors, in: K. Wandelt (Ed.) Encyclopedia of Interfacial Chemistry, Elsevier, Oxford, 2018, pp. 164–171.
[12] B. Vaghefinazari, E. Wierzbicka, P. Visser, R. Posner, R. Arrabal, E. Matykina, M. Mohedano, C. Blawert, M.L. Zheludkevich, S.V. Lamaka, Chromate-free corrosion protection strategies for magnesium alloys-a review: part iii-corrosion inhibitors and combining them with other protection strategies, Materials 15 (2022).
[13] J. Yang, P. Jiang, Y. Qiu, C.-Y. Jao, C. Blawert, S. Lamaka, A. Bouali, X. Lu, M. L. Zheludkevich, W. Li, Experimental and quantum chemical studies of carboxylates as corrosion inhibitors for AM50 alloy in pH neutral NaCl solution, J. Magnes. Alloy. (2021).
[14] J. Hu, D. Zeng, Z. Zhang, T. Shi, G.-L. Song, X. Guo, 2-Hydroxy-4-methoxy-acetophenone as an environment-friendly corrosion inhibitor for AZ91D magnesium alloy, Corros. Sci. 74 (2013) 35–43.
[15] A. Frignani, V. Grassi, F. Zanotto, F. Zucchi, Inhibition of AZ31 Mg alloy corrosion by anionic surfactants, Corros. Sci. 63 (2012) 29–39.
[16] J. Chen, J. He, L. Li, Spectroscopic insight into the role of SDBS on the interface evolution of Mg in NaCl corrosive medium, Corros. Sci. 182 (2021).
[17] Y. Chen, L. Wu, W. Yao, J. Wu, M. Serdechnova, C. Blawert, M.L. Zheludkevich, Y. Yuan, Z. Xie, F. Pan, Smart" micro/nano container-based self-healing coatings on magnesium alloys: a review, J. Magnes. Alloy. 11 (2023) 2230–2259.
[18] B. Vaghefinazari, E. Wierzbicka, P. Visser, R. Posner, R. Arrabal, E. Matykina, M. Mohedano, C. Blawert, M. Zheludkevich, S. Lamaka, Chromate-free corrosion protection strategies for magnesium alloys-a review: PART I-pre-treatment and conversion coating, Materials (15 () (2022).
[19] L.M. Calado, M.G. Taryba, Y. Morozov, M.J. Carmezim, M.F. Montemor, Novel smart and self-healing cerium phosphate-based corrosion inhibitor for AZ31 magnesium alloy, Corros. Sci. 170 (2020).
[20] G. Williams, N. Birbilis, H.N. McMurray, Controlling factors in localised corrosion morphologies observed for magnesium immersed in chloride containing electrolyte, Faraday Discuss. 180 (2015) 313–330.
[21] M. Liu, P.J. Uggowitzer, A.V. Nagasekhar, P. Schmutz, M. Easton, G.-L. Song, A. Atrens, Calculated phase diagrams and the corrosion of die-cast Mg–Al alloys, Corros. Sci. 51 (2009) 602–619.
[22] L. Yang, X. Zhou, S.-M. Liang, R. Schmid-Fetzer, Z. Fan, G. Scamans, J. Robson, G. Thompson, Effect of traces of silicon on the formation of Fe-rich particles in pure magnesium and the corrosion susceptibility of magnesium, J. Alloy. Compd. 619 (2015) 396–400.
[23] D. Hoche, C. Blawert, S.V. Lamaka, N. Scharnagl, C. Mendis, M.L. Zheludkevich, The effect of iron re-deposition on the corrosion of impurity-containing magnesium, Phys. Chem. Chem. Phys. 18 (2016) 1279–1291.
[24] D. Mercier, J. Światowska, S. Zanna, A. Seyeux, P. Marcus, Role of segregated iron at grain boundaries on Mg corrosion, J. Electrochem. Soc. 165 (2018) C42–C49.
[25] D. Mercier, J. Światowska, E. Protopopoff, S. Zanna, A. Seyeux, P. Marcus, Inhibition of Mg corrosion by sulfur blocking of the hydrogen evolution reaction on iron impurities, J. Electrochem. Soc. 167 (2020).
[26] S.V. Lamaka, D. Höche, R.P. Petrauskas, C. Blawert, M.L. Zheludkevich, A new concept for corrosion inhibition of magnesium: suppression of iron re-deposition, Electrochem. Commun. 62 (2016) 5–8.
[27] A. Maltseva, S.V. Lamaka, K.A. Yasakau, D. Mei, D. Kurchavov, M.L. Zheludkevich, G. Lefèvre, P. Volovitch, In situ surface film evolution during Mg aqueous corrosion in presence of selected carboxylates, Corros. Sci. 171 (2020).
[28] Y. Cui, T. Zhang, F. Wang, New understanding on the mechanism of organic inhibitors for magnesium alloy, Corros. Sci. 198 (2022).
[29] A.D. John, Lange's handbook of chemistry, in: Universitas Of Tennese Knoxville, Fifthenth Edition, Mc. Graw Hill Inc, New York. Conference, 1999.
[30] J. Yang, C. Blawert, S.V. Lamaka, K.A. Yasakau, L. Wang, D. Laipple, M. Schieda, S. Di, M.L. Zheludkevich, Corrosion inhibition of pure Mg containing a high level of iron impurity in pH neutral NaCl solution, Corros. Sci. 142 (2018) 222–237.
[31] B. Vaghefinazari, C. Wang, D. Mercier, D. Mei, A. Seyeux, P. Marcus, C. Blawert, S. V. Lamaka, M.L. Zheludkevich, Adverse effect of 2,5PDC corrosion inhibitor on PEO coated magnesium, Corros. Sci. 192 (2021).
[32] G. Zhang, E. Jiang, L. Wu, W. Ma, H. Yang, A. Tang, F. Pan, Corrosion protection properties of different inhibitors containing PEO/LDHs composite coating on magnesium alloy AZ31, Sci. Rep. 11 (2021) 2774.
[33] K. Asami, K. Hashimoto, S. Shimodaira, XPS determination of compositions of alloy surfaces and surface oxides on mechanically polished iron-chromium alloys, Corros. Sci. 17 (1977) 713–723.
[34] K. Asami, S. Ono, Quantitative X-ray photoelectron spectroscopy characterization of magnesium oxidized in air, J. Electrochem. Soc. 147 (2000) 1408.
[35] J.H. Scofield, Hartree-Slater subshell photoionization cross-sections at 1254 and 1487 eV, J. Electron Spectrosc. Relat. Phenom. 8 (1976) 129–137.
[36] S. Tanuma, C.J. Powell, D.R. Penn, Calculations of electron inelastic mean free paths for 31 materials, Surf. Interface Anal. 11 (1988) 577–589.
[37] H. Shinotsuka, S. Tanuma, C.J. Powell, D.R. Penn, Calculations of electron inelastic mean free paths. X. Data for 41 elemental solids over the 50 eV to 200 keV range with the relativistic full Penn algorithm, Surf. Interface Anal. 47 (2015) 871–888.
[38] N. Schell, A. King, F. Beckmann, T. Fischer, M. Müller, A. Schreyer, The high energy materials science beamline (HEMS) at PETRA III, Mater. Sci. Forum 772 (2013) 57–61.
[39] D. Mei, S.V. Lamaka, C. Feiler, M.L. Zheludkevich, The effect of small-molecule bio-relevant organic components at low concentration on the corrosion of commercially pure Mg and Mg-0.8Ca alloy: an overall perspective, Corros. Sci. 153 (2019) 258–271.
[40] L. Wang, T. Shinohara, B.-P. Zhang, XPS study of the surface chemistry on AZ31 and AZ91 magnesium alloys in dilute NaCl solution, Appl. Surf. Sci. 256 (2010) 5807–5812.
[41] M.P. Gomes, I. Costa, N. Pébère, J.L. Rossi, B. Tribollet, V. Vivier, On the corrosion mechanism of Mg investigated by electrochemical impedance spectroscopy, Electrochim. Acta 306 (2019) 61–70.
[42] L. Wang, D. Snihirova, M. Deng, C. Wang, B. Vaghefinazari, G. Wiese, M. Langridge, D. Höche, S.V. Lamaka, M.L. Zheludkevich, Insight into physical interpretation of high frequency time constant in electrochemical impedance spectra of Mg, Corros. Sci. 187 (2021).
[43] M. Santamaria, F. Di Quarto, S. Zanna, P. Marcus, Initial surface film on magnesium metal: a characterization by X-ray photoelectron spectroscopy (XPS) and photocurrent spectroscopy (PCS), Electrochim. Acta 53 (2007) 1314–1324.
[44] Z. Xu, U. Eduok, A.A. Tiamiyu, J. Szpunar, Anodic dissolution pattern of magnesium alloy in different media: effects of solution treatment on its microstructure and corrosion behaviour, Eng. Fail. Anal. 107 (2020).
[45] A. Seyeux, M. Liu, P. Schmutz, G. Song, A. Atrens, P. Marcus, ToF-SIMS depth profile of the surface film on pure magnesium formed by immersion in pure water and the identification of magnesium hydride, Corros. Sci. 51 (2009) 1883–1886.
[46] H. Ardelean, A. Seyeux, S. Zanna, F. Prima, I. Frateur, P. Marcus, Corrosion processes of Mg–Y–Nd–Zr alloys in Na2SO4 electrolyte, Corros. Sci. 73 (2013) 196–207.
[47] W. Jeffrey Binns, F. Zargarzadah, V. Dehnavi, J. Chen, J.J. Noël, D.W. Shoesmith, Physical and electrochemical evidence for the role of a Mg hydride species in Mg alloy, Corrosion, Corrosion 75 (2019) 58–68.
[48] N. Birbilis, T. Cain, J.S. Laird, X. Xia, J.R. Scully, A.E. Hughes, Nuclear microprobe analysis for determination of element enrichment following magnesium dissolution, ECS Electrochem. Lett. 4 (2015) C34–C37.
[49] T. Cain, S.B. Madden, N. Birbilis, J.R. Scully, Evidence of the enrichment of transition metal elements on corroding magnesium surfaces using rutherford backscattering spectrometry, J. Electrochem. Soc. 162 (2015) C228–C237.
[50] G. Balducci, L. Bravo Diaz, D.H. Gregory, Recent progress in the synthesis of nanostructured magnesium hydroxide, CrystEngComm 19 (2017) 6067–6084.
[51] X. Huang, L. Yu, Y. Dong, Corrosion resistance of a novel ceria doped aluminum phosphate ceramic coating on cast Al-Si alloy by steam-assisted curing, Corros. Sci. 182 (2021).
[52] C. Wang, D. Mei, G. Wiese, L. Wang, M. Deng, S.V. Lamaka, M.L. Zheludkevich, High rate oxygen reduction reaction during corrosion of ultra-high-purity magnesium, npj Mater. Degrad. 4 (2020).

[53] M. Strebl, S. Virtanen, Real-time monitoring of atmospheric magnesium alloy corrosion, J. Electrochem. Soc. 166 (2018) C3001–C3009.
[54] C. Wang, W. Xu, D. Höche, M.L. Zheludkevich, S.V. Lamaka, Exploring the contribution of oxygen reduction reaction to Mg corrosion by modeling assisted local analysis, J. Magnes. Alloy. (2022).
[55] E.L. Silva, S.V. Lamaka, D. Mei, M.L. Zheludkevich, The reduction of dissolved oxygen during magnesium corrosion, ChemistryOpen 7 (2018) 664–668.
[56] D. Snihirova, M. Taryba, S.V. Lamaka, M.F. Montemor, Corrosion inhibition synergies on a model Al-Cu-Mg sample studied by localized scanning electrochemical techniques, Corros. Sci. 112 (2016) 408–417.
[57] A. Maltseva, V. Shkirskiy, G. Lefèvre, P. Volovitch, Effect of pH on Mg(OH)2 film evolution on corroding Mg by in situ kinetic Raman mapping (KRM), Corros. Sci. 153 (2019) 272–282.
[58] P. Taheri, J.H.W. de Wit, H. Terryn, J.M.C. Mol, In situ study of buried metal–polymer interfaces exposed to an aqueous solution by an integrated ATR-FTIR and electrochemical impedance spectroscopy system, J. Phys. Chem. C. 117 (2013) 20826–20832.
[59] P. Taheri, M. Ghaffari, J.R. Flores, F. Hannour, J.H.W. de Wit, J.M.C. Mol, H. Terryn, Bonding mechanisms at buried interfaces between carboxylic polymers and treated zinc surfaces, J. Phys. Chem. C. 117 (2013) 2780–2792.
[60] I. Milošev, T. Bakarič, S. Zanna, A. Seyeux, P. Rodič, M. Poberžnik, F. Chiter, P. Cornette, D. Costa, A. Kokalj, P. Marcus, Electrochemical, surface-analytical, and computational DFT study of alkaline etched aluminum modified by carboxylic acids for corrosion protection and hydrophobicity, J. Electrochem. Soc. 166 (2019) C3131–C3146.
[61] G.A. Parks, The isoelectric points of solid oxides, solid hydroxides, and aqueous hydroxo complex systems, Chem. Rev. 65 (1965) 177–198.
[62] V.A. Phillips, J.L. Kolbe, H. Opperhauser, Effect of pH on the growth of Mg(OH)2 crystals in an aqueous environment at 60°C, J. Cryst. Growth 41 (1977) 228–234.
[63] A.D. King, N. Birbilis, J.R. Scully, Accurate electrochemical measurement of magnesium corrosion rates; a combined impedance, mass-loss and hydrogen collection study, Electrochim. Acta 121 (2014) 394–406.